Copper accelerates photochemically induced radical chemistry of iron-containing SOA

Kevin Kilchhofer[1,2,3], Markus Ammann[1], Laura Torrent[1,4,5], Rico K. Y. Cheung[1,6], and Peter A. Alpert[1,7]

[1]PSI Center for Energy and Environmental Sciences, 5232 PSI Villigen, Switzerland

[2]Department of Environmental System Science, Institute for Atmospheric and Climate Science, ETH Zurich, 8092 Zurich, Switzerland

[3]now at: Physikalisch Meteorologisches Observatorium, World Radiation Center (PMOD/WRC), 7260 Davos, Switzerland

[4]School of Architecture, Civil, and Environmental Engineering (ENAC IIE GR-LUD), École Polytechnique Fédérale de Lausanne (EPFL), 1015 Lausanne, Switzerland

[5]now at: Department of Chemistry, Faculty of Sciences, University of Girona, 17003 Girona, Spain

[6]now at: Department of Environmental Sciences, University of Basel, 4056 Basel, Switzerland

[7]now at: XRnanotech, 5232 Villigen PSI, Switzerland

Correspondence: Kevin Kilchhofer (kevin.kilchhofer@psi.ch) and Markus Ammann (markus.ammann@psi.ch)

Abstract. Photochemical aging in secondary organic aerosol (SOA) particles alters their chemical composition and affects their adverse health effects. However, there is limited mechanistic insight on the role of transition metals in photochemical SOA aging and the evolution of the oxidative potential through their effect on radical chemistry. Here, we investigated the influence of copper (Cu) on the photochemical aging of iron (Fe) containing SOA in single particles using scanning transmission X-ray microscope measurements and chemical box modeling. The SOA proxy included citric acid (CA), iron(III) citrate ($Fe^{III}(Cit)$) and copper(II) citrate ($Cu^{II}(HCit)$), which were exposed to UV light ($\lambda = 365\,\mathrm{nm}$) in a humidified environmental cell. We modeled known catalytic radical destruction mechanisms resulting from cross-redox reactions between copper and iron. Simulating anoxic $Fe^{III}(Cit)/Cu^{II}(HCit)/CA$ aging experiments showed a lower initial iron(III) reduction compared to $Fe^{III}(Cit)/CA$ particles, indicating a reduced iron(II) quantum yield than the photolysis of the $Fe^{III}(Cit)$ alone. We hypothesize that this effect may be due to copper replacing an iron center in a polynuclear complex. At higher relative humidity (RH) up to 60%, a lower iron(II) quantum yield could not account for our observations of iron reoxidation in the dark. Instead, reoxidation appears to be highly sensitive to a potential copper(II)-induced reoxidation reaction. We provide a comprehensive discussion and evaluation of the poorly understood role of copper in modifying redox and radical chemistry, which is relevant for reactions involving transition metals mixed with SOA in the atmosphere.

1 Introduction

Secondary organic aerosol (SOA) particles are a major component of tropospheric particulate matter (PM), predominantly formed through the oxidation of biogenic and anthropogenic volatile organic compounds (Hallquist et al., 2009). Consequently, SOA particles consist of various molecules from different precursor gases, which greatly influence atmospheric chemistry (Pöschl and Shiraiwa, 2015). Due to their substantial mass yield, SOA particles are significant contributors to particulate air pollution (Huang et al., 2015). The health impacts of PM are suggested to be related to the concentration of reactive oxygen species (ROS), such as hydroxy radicals or hydroperoxides (Weichenthal et al., 2019; Shiraiwa et al., 2023). ROS can be introduced into the body through inhalation of PM (particle-bound ROS) (Dellinger et al., 2001) or catalytically generated in vivo after inhalation by redox-active PM species (semi-empirically quantified by oxidative potential, or OP) (Bates et al., 2019). For example, particle-bound ROS have been associated with fine-mode SOA particles and with coarse-mode metals from vehicular non-exhaust emissions (Daellenbach et al., 2020). SOA particles nucleated from the oxidation products of biogenic volatile organic compounds (VOC) can mix with primary emitted aerosol particles (e.g. mineral dust), which contain redox-active components such as transition metal ions (Charrier and Anastasio, 2015). This mixing has been found to enhance ROS production by these particles (Tuet et al., 2017; Alpert et al., 2021).

Transition metal ions, such as iron and copper, have long been known to dissolve in atmospheric liquid phases (Kieber et al., 2001; Deguillaume et al., 2005). Natural emissions from dust regions and anthropogenic activities, such as traffic and combustion, are primary sources of soluble iron (Ito and Miyakawa, 2023), making it the most abundant metal in the atmosphere. Copper emissions increased greatly during the industrial revolution (Hong et al., 1996), and the atmospheric copper concentration have been measured up to one-tenth of ambient iron concentration (Schroeder et al., 1987). In megacities, higher metal concentrations lead to increased levels of soluble iron and copper in PM (Chifflet et al., 2024). In SOA, dissolved metals form complexes with organic material (Moffet et al., 2012; Al-Abadleh, 2015, 2024). Field studies have shown that soluble iron occurs mainly in complexes with carboxylate functional groups (Tapparo et al., 2020; Tao and Murphy, 2019) and both iron and copper complexes have been identified in ambient PM, indicating a significant alteration of their OP (Wei et al., 2019).

Due to the long atmospheric lifetimes, aging processes can significantly alter the physicochemical properties of SOA particles (Kroll and Seinfeld, 2008; Robinson et al., 2007). Photochemistry plays a central role in many aerosol aging processes (George et al., 2015). In the condensed phase, photochemical reactions are more easily initiated compared to the gas phase, as photoexcited species are in closer proximity to energy or electron acceptors. Organometallic complexes often have a high UV absorption cross section, leading to indirect photochemistry (George et al., 2015; Corral Arroyo et al., 2018). We hypothesize that particles containing iron, copper, and SOA undergo photochemical reactions subsequently producing ROS. This study aims to quantify the redox chemistry of these transition metals and further elucidate the photochemical reaction mechanism, shedding light on new pathways of ROS formation in SOA.

Citric acid (CA) is commonly used as a model system for SOA due to its oxygen to carbon ratio (O:C) and atmospherically relevant viscosity properties (Reid et al., 2018; Dou et al., 2021; Alpert et al., 2021; Wang et al., 2023). Iron citrate ($Fe^{III}Cit$) is a representative iron-carboxylate complex with reasonably well-characterized photochemistry (Cieśla et al., 2004; Wang
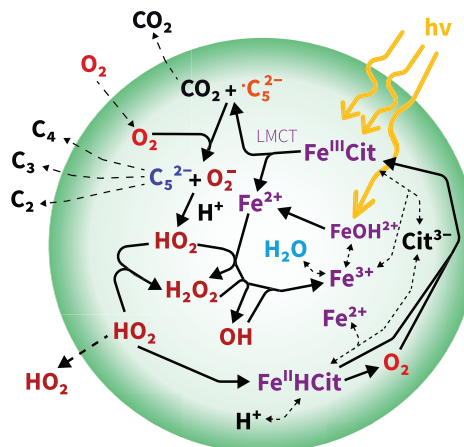
Figure 1. Schematic of photochemically induced $Fe^{III}(Cit)$/CA chemistry in a viscous particle. The detailed mechanism, including equilibria and reaction rates, is outlined in Tables 1, 2 and 3. $^{\bullet}C_5^{2-}$ denotes the carbon-centered free radical $^{\bullet}C_5H_5O_5^{2-}$, while C_5^{2-} refers to the ketoacid $C_5H_4O_5^{2-}$ in reactions E8, R1 and R2. $Fe^{III}Cit$ denotes $FeC_6H_5O_7$, $Fe^{II}HCit$ corresponds to $FeC_6H_6O_7^{2-}$, and Cit^{3-} refers to $C_6H_5O_7^{3-}$. LMCT stands for ligand-to-metal charge transfer.

et al., 2012; Weller et al., 2013, 2014; Dou et al., 2021). Its high absorbance in the UV-visible range (Seraghni et al., 2012;
50 Abida et al., 2012) enables $Fe^{III}Cit$ to initiate condensed phase radical processes at wavelengths that most oxidized organic compounds (non-carbonyl) would not absorb on their own.

The number of citrate ligands per iron center, as well as the abundance of polynuclear (thus poly-iron) complex aggregates varies depending on pH and the ratio between CA and Fe^{III}(Abrahamson et al., 1994; Silva et al., 2009; Gracheva et al., 2022), with each species exhibiting different absorbance. In the following, we shorty outline the main $Fe^{III}Cit$ photochemical
55 mechanism shown in Figure 1 initiated by ligand-to-metal charge transfer (LMCT, violet), generating a reduced radical complex as the first intermediate (Glebov et al., 2011; Pozdnyakov et al., 2014). This may decompose into Fe^{II} and a citrate radical, which rapidly decarboxylates at the central carboxyl group, releasing CO_2 and forming a carbon-centered free radical ($^{\bullet}C_5^{2-}$, orange in Figure 1) (Weller et al., 2013). In the presence of O_2, ROS species, HO_2 and O_2^-, and a ketoacid (C_5^{2-}, blue in Figure 1) are produced. The ketoacid can also form through the reaction of the citrate radical or the reduced radical complex with
60 $Fe^{III}Cit$, or by reaction with another Fe^{III} center within the same polynuclear complex (Abrahamson et al., 1994; Glebov et al., 2011). These additional pathways yield a second Fe^{II} without producing ROS, potentially leading to a higher apparent iron(II) quantum yield (ϕ). Iron(II) can be reoxidized to iron(III) with ROS via the Fenton reaction cycle (Fenton, 1894). Iron(III) subsequently combines with another CA molecule to form a new $Fe^{III}Cit$ complex, completing the photocatalytic cycle. This photodegradation process is also an important sink of carboxylate groups, and prolonged irradiation may result in the formation
65 of Fe-carbonaceous colloids, as recently reported by West et al. (2023). In more detail, with respect to the quantum yield, for different aqueous iron(III) polycarboxylate complexes, including Fe^{III}(Cit), ϕ, varies with solution composition, pH and with

the presence or not of O_2. Faust and Zepp (1993) found a ϕ value of 0.28 in air for $Fe^{III}(Cit)$ complexes. Characterizing a series of environmentally relevant iron(III) carboxylate complexes at multiple wavelengths in the actinic spectrum, Weller et al. (2013) confirmed a range for ϕ between 0.2 and 0.6.This relatively low ϕ under various environmental conditions may be due to the

70 possibility of back-electron transfer of the reduced iron(II) radical complex intermediate (Glebov et al., 2011; Pozdnyakov et al., 2014). Abrahamson et al. (1994) found photoreduction in crystalline $Fe^{III}(Cit)$, but not in acetonitrile solution without water, highlighting the need for water. Abrahamson et al. (1994) measured ϕ in solution for various carboxylic acid proxies at different pH and initial metal-to-ligand ratios. For $Fe^{III}(Cit)$, over the pH range from 4 to 2, they observed ϕ decreasing from around 0.4 to around 0.1, while when increasing the iron(III) to ligand ratio from 0.02 to 0.5 at pH = 3, ϕ increased from 0.2 to

75 0.45. This was attributed to the formation of dimeric photoactive $Fe^{III}(Cit)$ species at high iron-to-ligand ratios. Therefore, the presence of dimeric or polymeric complexes, formed through paramagnetic coupling among Fe centers via oxygen bridges, as well as the presence of water, seems crucial for both absorbance and ϕ, which will be discussed in this work.

The formation of various ROS species, primarily driven by the generation of peroxy radicals, relies on O_2 supplied from the gas phase. Since O_2 has relatively low solubility, its availability can become rate limiting (Alpert et al., 2021), especially

80 when SOA particles become highly viscous at low relative humidity (RH) and/or temperatures (Virtanen et al., 2010; Koop et al., 2011). Under these anoxic conditions within the particle bulk, highly reactive species generated by photochemistry can accumulate. Upon humidification to higher RH, the increase O_2 uptake enhances the formation of additional ROS (Alpert et al., 2021). This work aims to bridge the gap between model SOA proxies and ambient SOA by investigating the role of relevant metal ions, specifically iron and copper, in the aerosol phase. The interactions between iron and other dissolved metals in

85 SOA, and their impact on particle-bound ROS production, remains unexplored. Previous studies on this subject have primarily focused on the role of metals in surrogate lung fluid in relation to their OP (Charrier et al., 2014; Wei et al., 2019; Lelieveld et al., 2021, 2024).

In this study, we introduce copper citrate ($Cu^{II}(HCit)$) to evaluate the influence of copper ions and organic complexes on the photochemical aging of $Fe^{III}(Cit)$/CA particles, thereby examining its role in aerosol aging, multiphase chemistry, and

90 particle-bound ROS formation. Using X-ray spectromicroscopy, we found that copper alters the photochemical aging process in $Fe^{III}(Cit)$/$Cu^{II}(HCit)$/CA particles, particularly in terms of iron reoxidation, compared to $Fe^{III}(Cit)$/CA particles studied by Alpert et al. (2021) without copper. This observation led us to model the photochemistry in $Fe^{III}(Cit)$/$Cu^{II}(HCit)$/CA particles and assess the importances of ROS-copper and iron-copper coupled reactions available from previous literature. In addition, the new reoxidation experiments could only be explained by adjusting the iron(II) quantum yield of $Fe^{III}(Cit)$ photolysis. We

95 suggest that copper may not only catalyze ROS cycling but also potentially replace iron in polymetal complexes, reducing the photolysis quantum yield and accelerating reoxidation in this system.

2 Material and Methods

2.1 STXM/NEXAFS for determining iron oxidation state.

Scanning transmission X-ray microscopy coupled with near-edge X-ray absorption fine structure (STXM/NEXAFS) spectroscopy (Raabe et al., 2008; Moffet et al., 2010) was used to determine the fraction of iron(III), β, out of the total iron after photoreduction and during in situ reoxidation in individual particles, following established methods (Alpert et al., 2019, 2021; Dou et al., 2021). The experiments were conducted at the PolLux beamline at the Swiss Light Source (SLS). NEXAFS spectra were also measured to quantify the oxidation states of both iron and copper. X-ray spectra were obtained by imaging particles at individual X-ray energies and then scanning across the energy range of relevant absorption edges. For iron, the energy was scanned from 700 to 735 eV, covering the L-edges around 709 and 721 eV, while for copper, the scan ranged from 925 to 965 eV to capture the $L_{2,3}$-edge peaks at 934 and 954 eV. For carbon, the energy was scanned from 278 to 318 eV to cover the C-K-edge NEXAFS region.

At different oxidation states, iron has a different L-edge peak position, occurring at, e.g. $\sim$ 707.8 and 709.6 eV for $FeCl_2$ and $FeCl_3$, respectively, with a separation of 1.8 eV (Moffet et al., 2012). This information was used to calibrate X-ray energy (Figure A1) with a constant offset. A mixture of the two oxidation states was quantified by first subtracting the background absorption at the iron pre-edge (between 700-705 eV, where iron does not absorb strongly), then taking the ratio of the absorption peak heights, and applying a previously established parameterization (Moffet et al., 2012; Dou et al., 2021; Alpert et al., 2019, 2021). All particles appeared homogeneous in terms of metal and organic distribution within all particles, meaning we never observed dense nanoparticles or gradients in Fe, Cu or organic concentration. However, we did observe gradients in oxidation state, and note that only Fe(II), Fe(III), Cu(I) and Cu(II) oxidation states were detected.

In order to quantify the iron oxidation states, we followed the procedure by Alpert et al. (2019), calculating the pre-edge absorption from a polynomial fit as a function of the sum of the absorption at the Fe(II) and Fe(III) peaks. Then, two high spatial resolution images with a pixel size of 35×35 nm^2 were acquired at the peak absorption energies for iron(II) and iron(III) at 710.1 and 711.9 eV, respectively (see Figure A1), allowing the calculation of β in the particles using Equation 1. The total iron(II) and iron(III) peak absorption energies to the concentration (C) of each specie in the particles. This fraction is then used to map the individual particles with a resolution of tens of nanometers, providing detailed spatial insights into their iron oxidation states.

$$\beta = \frac{C(Fe^{3+})}{C(Fe^{2+}) + C(Fe^{3+})} \tag{1}$$

When determining β, calculations were performed for each pixel in the images of particles, with uncertainties stemming from photon counting statistics, nanometer scale drift in positioning, automated image alignment, and errors from the iron pre-edge calculation (prediction error at 95% confidence). Radial profiles of β were obtained by averaging concentric pixels on and from the perimeter of the imaged particles (Alpert et al., 2019). The uncertainty in β was determined to be either $\Delta\beta = \pm 0.07$, or propagated from the photon counting error, whichever was larger. Two experimental procedures were utilized to investigate photochemical reduction and reoxidation over time. In the first, particles were generated from a Fe^{III}(Cit)/CuCl$_2$/CA solution,

placed under vacuum, and exposed to UV light. In the second, particles were generated from a solution containing $Cu^{II}(HCit)$ and placed in an environmental cell with controlled light exposure, RH, and O_2 concentration. When the humidity (and thus particle water content), O_2, or copper content was varied, the iron pre-edge absorption of the particles was different. Prior to light exposure for each experiment, background absorption at $700\,eV$ and the two absorption peaks for iron(II) and iron(III) were measured for about 100 particles. This data was used to create a unique polynomial fit for background absorption prior to UV exposure. As previously mentioned, the background absorption image was calculated from the fit, reducing the number of images from three to two in order to decrease the time needed to quantify β maps (Alpert et al., 2021).

2.2 Solutions and sample preparation

Particles for STXM/NEXAFS analysis were prepared by nebulizing the solutions using a custom-built ultrasonic nebulizer (Steimer et al., 2015). The nebulized particles were then dried at RH $\leq$ 30%, and directed to a single jet impactor in a N_2 flow, following passage through a differential mobility analyzer to select a dry mobility diameter of 300-400 nm. The particles were nebulized for $50\text{-}100\,s$ to ensure a homogeneously distributed sample with particles of 0.2-1 μm in diameter. We prepared six different solutions. Three had a 1:1 mole ratio of $Fe^{III}(Cit):CA$, two with mole ratios of $Cu^{II}(HCit):Fe^{III}(Cit) = 0.2$ and 0.02, and one with a mole ratio of $Cu^{II}Cl_2:Fe^{III}(Cit) = 0.2$. These ratios were chosen to replicate $Fe^{III}(Cit)/CA$ experiments from Alpert et al. (2021) and to evaluate atmospherically relevant copper concentrations, approximately one-tenth of the iron concentration (Schroeder et al. (1987); Wei et al. (2019). CA ($\geq$ 99.5%; CAS = 5949-29-1), $Fe^{III}(Cit)$ tribasic monohydrate (18-20% Fe basis; CAS = 2338-05-8) and $Cu^{II}(HCit)$ (97%; CAS = 866-82-0) were purchased from Sigma-Aldrich. The dilute aqueous solutions were prepared in ultrapure water (18 MΩ cm^{-1}, Milli-Q). The measured pH $\approx$ 2 of the solutions did not differ between the different mole ratios. Because we only sampled a very low mass of particles, we were unable to measure the pH after a STXM experiment. The solution was then nebulized, and the particles were impacted on silicon nitride windows, which were then sealed inside replaceable sample holders compatible with the environmental cell used for the STXM/NEXAFS (Alpert et al., 2021; Huthwelker et al., 2010). The viscosity of the particles at the same RH did not vary between different particle compositions as the concentrations of iron was too low to influence the viscosity of CA as proven by Alpert et al. (2021), while we assume that the small amount of additional copper did not change that.

2.3 STXM environmental cell and photochemical reactor

In the environmental cell, the iron oxidation state was mapped in situ in the dark following photolysis (Alpert et al., 2021; Huthwelker et al., 2010). The particle samples were first transported under vacuum to the PolLux endstation at the SLS, where they were loaded into the environmental cell. During preparation, transport and loading, all ambient room light was switched off, and efforts were made to shield the samples and the solutions from any additional light, ensuring minimal light exposure before sealing the end station. The interval between impaction and X-ray investigation was approximately two hours. The environmental cell maintained a controlled gas flow with constant RH ranging from 0-60 % and O_2 at partial pressure adjusted according to the desired RH. Helium served as the carrier gas for O_2 and H_2O with a total flow rate of $20\,mL\,min^{-1}$ (stp). At RH = 60%, 50% and 40%, the oxygen to helium flow ratios were 0.6, 0.75 and 0.8, respectively.
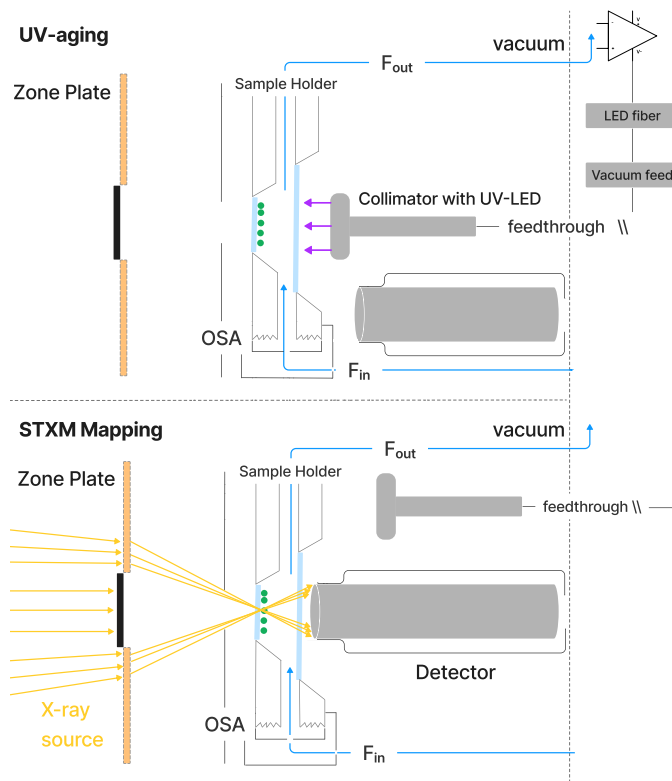
Figure 2. Schematic of the environmental cell situated inside the STXM/NEXAFS vacuum chamber. During UV-aging, the particles (green dots) on the silicon nitride (SiNit) membranes were aligned with a UV-LED collimator. For STXM/NEXAFS analysis, the collimator was moved aside and an X-ray detector was moved in its place. SiNit membranes were sealed in an aluminium sample holder, which was attached to the aluminium environmental cell sealed with an O-ring. A constant, humid helium flow (blue line) was maintained through the environmental cell. The positions of the detector and collimator were automatically alternated between the two experimental conditions.

Figure 2 shows a schematic of the UV-LED fiber optic system used for UV-aging experiments in the STXM. The system includes a LED (LuxiGenTM $365\,\mathrm{nm}$ UV LED Gen 4 Emitter, Model LZ1-00UV0R) and two interchangeable collimators (Thorlabs, model CFC-2X-A and model CFC-5X-A), which provide uniform illumination throughout the sample area. The power density can be adjusted between $(2.36 \pm 0.06)\,\mathrm{W\,m^{-2}}$ and $(13.55 \pm 0.06)\,\mathrm{W\,m^{-2}}$) over a narrow wavelength range of 360-380 nm (with a full-width half-maximum of approximately $20\,\mathrm{nm}$). This corresponds to a photolysis frequency for $\mathrm{Fe^{III}(Cit)}$, j_{FeCit}, ranging from $(1.4 \pm 0.2) \times 10^{-3}\,\mathrm{s^{-1}}$ to $(8.1 \pm 0.9) \times 10^{-3}\,\mathrm{s^{-1}}$. Light intensity was regulated by a dimmer circuit, which was controlled by an electrical signal ranging from 1 to 7 V. The fiber optics, with a numerical aperture of 0.5 and a core diameter of $1000\,\mu\mathrm{m}$, allowed for a large acceptance angle, ensuring sufficient light transmission from the LEDs. The fiber is multimode and has a high OH content, which ensures transmission of ultraviolet and visible light with minimal loss. A custom-built vacuum feed through connected the fiber optics to the STXM chamber. The spectral flux density of the

light as a function of wavelength was measured after the collimator using a pre-calibrated power meter (Air-Cooled Thermopile Sensors, Model PM2) and spectrometer (Avantes, model AvaSpec-ULS2048XL-EVOis).

2.4 Photolysis frequency

We compared the photolysis frequency of $Fe^{III}(Cit)$, j_{FeCit}, when illuminated by the LED light, to the actinic flux in Los Angeles at sea level for June $(E_{QF}(\lambda)_{sun})$ and December days. The actinic flux data was obtained using the *libRadtran* software (Emde et al., 2016), with the following parameters, albedo = 0.1, aerosol optical depth, $\tau = 0.1$, single scattering albedo (SSA) = 0.85, solar zenith angle (SZA) = 23.4° and O_3 column = 300 DU. The corresponding spectra can be seen in Figure B1) in the SI. At noon in June, the photolysis frequency in Los Angeles is $j = (2.9 \pm 0.2) \times 10^{-2}\,s^{-1}$, integrated over the 270-500 nm wavelength range. The UV-aging of $Fe^{III}(Cit):Cu^{II}(HCit):CA$ particles under atmospheric conditions scales in proportion to j calculated from the LED flux, the absorption cross section, and an iron(II) quantum yield, ϕ, of 1. For the wavelength range emitted by the LED (350-400 nm), j_{LED} reaches $(8.1 \pm 0.1) \times 10^{-3}\,s^{-1}$.

Using an equation derived by Malecha and Nizkorodov (2016) (Eq. 2) we compared j under atmospheric conditions, with the LED spectrum for two wavelength ranges, 350-400 nm and 270-500 nm. The resulting factor, ζ, is approximately 3.6 using the 350-400 nm range, at the lowest LED dimmer setting of 1 V. This indicates that the photochemical cycling with the LED light should be slower compared to ambient sunlight. We calculated ζ for the two LED dimmer settings (1 and 7 V), for both summer and winter sunlight conditions, and for the two wavelength ranges. These results are shown in Table B1 in the SI. For example, a LED-UV exposure of 10-15 min at 7 V is approximately 4-8 min sunlight exposure during summer in Los Angeles.

$$\zeta = \frac{\int_{\lambda_1}^{\lambda_2} E_{QF}(\lambda)_{sun} \cdot d\lambda}{\int_{\lambda_1}^{\lambda_2} E_{QF}(\lambda)_{LED} \cdot d\lambda} \tag{2}$$

2.5 Kinetic model of reoxidation in the $Fe^{III}(Cit)$/CA system

A kinetic box model (Kintecus solver package V2021, Ianni (2017)) was used to simulate the photochemical reduction and reoxidation of iron under variable RH, both with and without copper. Kintecus is a homogeneous phase-box model, which means that it does not account for inhomogeneity within particles. The model includes reactions, species description, and parameter descriptions designed to replicate the flow conditions in the STXM environmental cell. A summary of the chemical mechanisms, equilibrium constants and reaction rate coefficients used in the model is presented in Tables 1, 2 and 3. Except for reaction R19, where the rate coefficient was adjusted from $k_r = 3.00 \pm 0.70$ to $1.50\,M^{-1}\,s^{-1}$ for better simulation performance, all reaction rate constants were taken from Gonzalez et al. (2017). The initial conditions for the chemical concentrations were calculated as detailed in Section E1 of the SI, with the initial β before UV irradiation based on STXM/NEXAFS experimental data. A constant acidity of pH = 2 was maintained.

The phase transfer of a molecule (M) from the gas to the aqueous phase, M(g) $\longrightarrow$ M(aq), was modeled with the rate $k_{M(g)\rightarrow(aq)} = 1/4\omega_M\gamma_M A_p/V_p$, where ω_M is the mean thermal velocity of M, and A_p/V_p is the surface to volume ratio of a particle. The reverse rate, M(aq) $\longrightarrow$ M(g), was modeled using Henry's law and given as
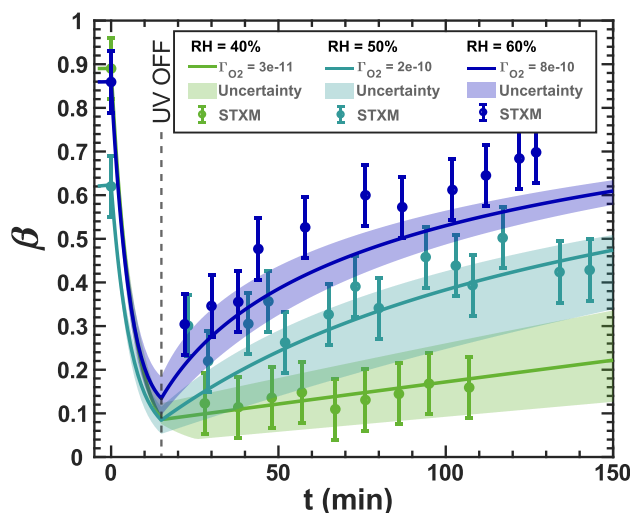
Figure 3. Iron(III) fraction, β, as a function of time, t, for 15 min of irradiation ($j = (1.4 \pm 0.2) \times 10^{-3} \, \text{s}^{-1}$) followed by a period of dark reoxidation under three humidity conditions. Each humidity scenario with a different oxygen uptake coefficients, Γ_{O_2}), is shows as green for RH = 40% and $\Gamma_{\text{O}_2} = (3 \pm 2) \times 10^{-11}$, turquoise for RH = 50% and $\Gamma_{\text{O}_2} = (2 \pm 1) \times 10^{-10}$, and blue for RH = 60% with $\Gamma_{\text{O}_2} = (8 \pm 6) \times 10^{-10}$). The circles with error bars are previous data (Dou et al., 2021), while the straight lines correspond to the output from the updated Kintecus model. The model uncertainty is the shaded area stemming from uncertainty in measured RH and light intensity.

$k_{\text{M(aq)} \to (g)} = k_{\text{M(g)} \to M(aq)}/(RTH_M)$. Chemical reactions and molecular diffusion can limit changes in particle composition

205 over time (Berkemeier et al., 2013), often leading to lower concentrations of species in the gas phase within particles than expected in equilibrium. In the case of rapid O_2 uptake and reaction with condensed phase molecules (reaction R2 in Table 3), O_2 maintains Henry's law equilibrium only near the particle surface, while its concentration rapidly decreases due to its reaction with abundant organic radicals. As our box model is non-depth resolving, the transfer of oxygen to the particle, Γ_{O_2}, was parameterized to account for this limitation. We treated Γ_{O_2} as an effective uptake coefficient parameterized as $\Gamma_{\text{O}_2} =$

210 $a_0 + a_1(1 - e^{-RH/a_2})$, where $a_0 = -20.0$, $a_1 = 12.40$ and $a_2 = 27.78$ based on fitting our results to those of the multilayer PRAD model (Dou et al., 2021). Although our box model does not account for molecular diffusion within particles, despite prior evidence of radial concentration gradients in $\text{Fe}^{\text{III}}(\text{Cit})$, it still serves as a useful tool to explore mechanistic scenarios, particularly how copper affects $\text{Fe}^{\text{III}}(\text{Cit})$ photochemistry. In future studies, a multilayer model informed by this work could be developed for a more detailed investigation.

215 Figure 3 shows previously published data from three separate reoxidation experiments with $\text{Fe}^{\text{III}}(\text{Cit}):\text{CA}$ particles at a $1:1$ mole ratio, conducted at RH = 60%, 50% and 40% as blue, turquoise, and green, respectively (Dou et al., 2021). Data points at $t = 0 \, \text{min}$ are measurements taken before UV irradiation and serve as the initial β values for each box model scenario. The box model results shown as lines agree well with the experimental data, taking into account the uncertainties in both the experimental data and the model, which mainly stems from variations in RH at $\pm 2\%$ and light intensity. Using these

220   results as a reference for the $Fe^{III}(Cit)$ system, we will adapt our box model in the results section to simulate the reduction and reoxidation of photochemically aged $Fe^{III}(Cit)/Cu^{II}(HCit)/CA$ particles and explore potential reaction mechanisms. The model uncertainties (colored area) stem from the uncertainty in RH of $\pm$ 2.5%, the light intensity, and the the oxygen uptake coefficient (Γ_{O_2}). This Γ_{O_2} was used in the model calculations to represent the change in particle viscosity at different RH.

Table 1. Chemical equilibria with equilibria constants (K_{eq}) and reaction rate constants (k_r) for forward and reverse reactions at pH = 2.

Nr.	Reactions	k_r	K_{eq}	References
E1	$H_2O \longrightarrow HO^- + H^+$	$2.34 \times 10^{-5}\,\mathrm{s}^{-1}$	$1.00 \times 10^{-14}\,\mathrm{M}$	Welch et al. (1969)
E1b	$HO^- + H^+ \longrightarrow H_2O$	$1.30 \times 10^{11}\,\mathrm{M}^{-1}\mathrm{s}^{-1}$		
E2	$H_2O_2 \longrightarrow HO_2^{\bullet} + H^+$	$1.26 \times 10^{-2}\,\mathrm{s}^{-1}$	$1.26 \times 10^{-12}\,\mathrm{M}$	De Laat and Le (2005)
E2b	$HO_2^- + H^+ \longrightarrow H_2O_2$	$1.00 \times 10^{10}\,\mathrm{M}^{-1}\mathrm{s}^{-1}$		
E3	$HO_2^{\bullet} \longrightarrow O_2^{\bullet-} + H^+$	$8.00 \times 10^{5}\,\mathrm{s}^{-1}$	$1.6 \times 10^{-5}\,\mathrm{M}^{-1}$	Bielski et al. (1985)
E3b	$O_2^{\bullet-} + H^+ \longrightarrow HO_2^{\bullet}$	$5.00 \times 10^{10}\,\mathrm{M}^{-1}\mathrm{s}^{-1}$		
E4	$C_6H_8O_7 \longrightarrow C_6H_7O_7^- + H^+$	$7.50 \times 10^{6}\,\mathrm{s}^{-1}$	$7.50 \times 10^{-4}\,\mathrm{M}$	Martell and Smith (1982)
E4b	$C_6H_7O_7^- + H^+ \longrightarrow C_6H_8O_7$	$1.00 \times 10^{10}\,\mathrm{M}^{-1}\mathrm{s}^{-1}$		
E5	$C_6H_7O_7^- \longrightarrow C_6H_6O_7^{2-} + H^+$	$1.70 \times 10^{5}\,\mathrm{s}^{-1}$	$1.70 \times 10^{-5}\,\mathrm{M}$	Martell and Smith (1982)
E5b	$C_6H_6O_7^{2-} + H^+ \longrightarrow C_6H_7O_7^-$	$1.00 \times 10^{10}\,\mathrm{M}^{-1}\mathrm{s}^{-1}$		
E6	$C_6H_6O_7^{2-} \longrightarrow C_6H_5O_7^{3-} + H^+$	$4.00 \times 10^{3}\,\mathrm{s}^{-1}$	$4.00 \times 10^{-7}\,\mathrm{M}$	Martell and Smith (1982)
E6b	$C_6H_5O_7^{3-} + H^+ \longrightarrow C_6H_6O_7^{2-}$	$1.00 \times 10^{10}\,\mathrm{M}^{-1}\mathrm{s}^{-1}$		
E7	$Fe^{3+} + C_6H_5O_7^{3-} \longrightarrow FeC_6H_5O_7$	$1.00 \times 10^{10}\,\mathrm{M}^{-1}\mathrm{s}^{-1}$	$1.58 \times 10^{13}\,\mathrm{M}$	Dou et al. (2021)
E7b	$FeC_6H_5O_7 \longrightarrow Fe^{3+} + C_6H_5O_7^{3-}$	$6.33 \times 10^{-4}\,\mathrm{s}^{-1}$		
E8	$Fe^{3+} + C_6H_6O_7^{2-} \longrightarrow FeC_6H_6O_7^+$	$1.00 \times 10^{10}\,\mathrm{M}^{-1}\mathrm{s}^{-1}$	$2.51 \times 10^{7}\,\mathrm{M}^{-1}$	Dou et al. (2021)
E8b	$FeC_6H_6O_7^+ \longrightarrow Fe^{3+} + C_6H_6O_7^{2-}$	$3.98 \times 10^{2}\,\mathrm{s}^{-1}$		
E9	$Fe^{2+} + C_6H_6O_7^{2-} \longrightarrow FeC_6H_6O_7$	$1.00 \times 10^{10}\,\mathrm{M}^{-1}\mathrm{s}^{-1}$	$1.94 \times 10^{10}\,\mathrm{M}^{-1}$	Dou et al. (2021)
E9b	$FeC_6H_6O_7 \longrightarrow Fe^{2+} + C_6H_6O_7^{2-}$	$5.17 \times 10^{-1}\,\mathrm{s}^{-1}$		
E10	$Fe^{2+} + C_5H_4O_5^{2-} \longrightarrow FeC_5H_4O_5$	$1.00 \times 10^{10}\,\mathrm{M}^{-1}\mathrm{s}^{-1}$	$2.00 \times 10^{3}\,\mathrm{M}^{-1}$	Dou et al. (2021)
E10b	$FeC_5H_4O_5 \longrightarrow Fe^{2+} + C_5H_4O_5^{2-}$	$5.00 \times 10^{6}\,\mathrm{s}^{-1}$		

Table 2. Table 1 continued.

Nr.	Reactions	k_r	K_{eq}	References
E11	$^\bullet C_5H_5O_5{}^{2-} + 2\,H^+ \longrightarrow {}^\bullet C_5H_7O_5$	$1.00 \times 10^{10}\,\mathrm{M^{-1}\,s^{-1}}$	$2.00 \times 10^3\,\mathrm{M^{-1}}$	Dou et al. (2021)
E11b	$^\bullet C_5H_7O_5 \longrightarrow {}^\bullet C_5H_5O_5{}^{2-} + 2\,H^+$	$6.67 \times 10^3\,\mathrm{s^{-1}}$		
E12	$C_5H_4O_5{}^{2-} + 2\,H^+ \longrightarrow C_5H_6O_5$	$1.00 \times 10^{10}\,\mathrm{M^{-1}\,s^{-1}}$	$2.00 \times 10^3\,\mathrm{M^{-1}}$	Dou et al. (2021)
E12b	$C_5H_6O_5 \longrightarrow C_5H_4O_5{}^{2-} + 2\,H^+$	$6.67 \times 10^3\,\mathrm{s^{-1}}$		
E13	$Fe^{3+} + H_2O \longrightarrow FeOH^{2+} + H+$	$4.7 \times 10^4\,\mathrm{M^{-1}\,s^{-1}}$	$1.10 \times 10^{-4}\,\mathrm{M^{-1}}$	Brandt and van Eldik (1995)
E13b	$FeOH^{2+} + H^+ \longrightarrow Fe^{3+} + H_2O$	$4.3 \times 10^8\,\mathrm{s^{-1}}$		
E14	$FeOH^{2+} + H_2O \longrightarrow [FeOH_2]^+ + H^+$	$1.10 \times 10^3\,\mathrm{M^{-1}\,s^{-1}}$	$1.40 \times 10^{-7}\,\mathrm{M^{-1}}$	Hemmes et al. (1971)
E14b	$[FeOH_2]^+ + H^+ \longrightarrow FeOH^{2+} + H_2O$	$8.00 \times 10^9\,\mathrm{s^{-1}}$		

3 Results and Discussion

3.1 Iron(III) reduction experiments

Figure 4 shows β under vacuum conditions (without O_2 and RH = 0). Light exposure resulted in the reduction of iron from its initial condition, both in the presence and absence of copper as $CuCl_2$, with a photolysis frequency, $j_{FeCit/CuCl2}$ = $(1.4 \pm 0.2) \times 10^{-3}\,\mathrm{s^{-1}}$. However, consistently higher values of β were observed compared to our model predictions at longer exposure times. Our box model reproduces measurements of iron reduction in the $Fe^{III}(Cit)/CA$ photochemical system, con- firming j used in previous experiments conducted under vacuum conditions, with ϕ = 1 Dou et al. (2021). This agreement suggests that the $Fe^{III}(Cit)/CuCl_2/CA$ system aligns with the calculated photochemical loss rate, until β falls below 0.2 at an exposure time of 17 min. Under vacuum conditions, both $Fe^{III}(Cit)$ alone or its mixture with $CuCl_2$ are expected to be present as crystalline or amorphous (glassy) solid, potentially phase separated or mixed phase. We also applied ϕ = 1 in the model shown in Figure C1. From these results, we conclude the following. First, $CuCl_2$ does not affect the initial photochem- ical reaction steps to reduce $Fe^{III}(Cit)$. Second, ϕ for the photochemical reduction between 345-385 nm for $Fe^{III}(Cit)/CA$ and $Fe^{III}(Cit)/CuCl_2/CA$ is between 0.9-1. Previous studies have reported photoreduction of pure crystalline $Fe^{III}(Cit)$ through ob- servation of CO_2 production (Abrahamson et al., 1994), indicating that the solid matrix does not impede iron(III) reduction. $\phi = 0.3$ has been reported for $Fe^{III}(Cit)$ in aqueous solutions (Pozdnyakov et al., 2014). Furthermore, Corral Arroyo et al. (2022) reported enhanced photoreduction in pure $Fe^{III}(Cit)$ particles through resonant nanofocusing. Although we did not im- age photoreduction hotspots (likely due to different optical properties or non-spherical shape of the mixed particles considered

Table 3. Chemical reactions with rate constants and photolysis frequencies used in Kintecus at pH = 2.

Number	Reactions	$K_{eq}/k_r/\sigma$	References
R1	$FeC_6H_5O_7 \xrightarrow{h\nu} Fe^{2+} + {}^\bullet C_5H_5O_5{}^{2-} + CO_2$	$2.20 \times 10^{-3}\,\mathrm{s^{-1}}$	Dou et al. (2021)
R2	${}^\bullet C_5H_5O_5{}^{2-} + O_2 \longrightarrow C_5H_4O_5{}^{2-} + O_2{}^{\bullet-} + H^+$	$1.00 \times 10^{6}\,\mathrm{M^{-1}\,s^{-1}}$	Hug et al. (2001)
	ROS Reactions:		
R3	$HO_2{}^\bullet + HO_2{}^\bullet \longrightarrow H_2O_2 + O_2$	$8.30 \times 10^{5}\,\mathrm{M^{-1}\,s^{-1}}$	Bielski et al. (1985)
R4	$HO^\bullet + HO^\bullet \longrightarrow H_2O_2$	$5.50 \times 10^{9}\,\mathrm{M^{-1}\,s^{-1}}$	Sehested et al. (1968)
R5	$HO_2^\bullet + HO^\bullet \longrightarrow H_2O + O_2$	$7.00 \times 10^{9}\,\mathrm{M^{-1}\,s^{-1}}$	Sehested et al. (1968)
R6	$HO^\bullet + O_2{}^{\bullet-} \longrightarrow HO^- + O_2$	$1.10 \times 10^{10}\,\mathrm{M^{-1}\,s^{-1}}$	Sehested et al. (1968)
R7	$H_2O_2 + O_2{}^{\bullet-} \longrightarrow HO_2{}^\bullet + H_2O$	$2.70 \times 10^{7}\,\mathrm{M^{-1}\,s^{-1}}$	Christensen et al. (1982)
R8	$HO_2{}^\bullet + O_2{}^{\bullet-} \xrightarrow{H^+} H_2O_2 + O_2$	$9.70 \times 10^{7}\,\mathrm{M^{-1}\,s^{-1}}$	Bielski et al. (1985)
	Fe(II)/(III) Oxidant Reactions:		
R9	$Fe^{2+} + O_2{}^{\bullet-} \xrightarrow{2H^+} Fe^{3+} + H_2O_2$	$1.00 \times 10^{7}\,\mathrm{M^{-1}\,s^{-1}}$	Rush and Bielski (1985)
R10	$Fe^{2+} + HO_2{}^\bullet \xrightarrow{H^+} Fe^{3+} + H_2O_2$	$1.20 \times 10^{6}\,\mathrm{M^{-1}\,s^{-1}}$	Jayson et al. (1973)
R11	$Fe^{2+} + HO^\bullet \longrightarrow FeOH^{2+}$	$4.30 \times 10^{8}\,\mathrm{M^{-1}\,s^{-1}}$	Christensen and Sehested (1981)
R12	$Fe^{2+} + H_2O_2 \longrightarrow Fe^{3+} + HO^\bullet + HO^-$	$76\,\mathrm{M^{-1}\,s^{-1}}$	Walling (1975)
R13	$Fe^{3+} + O_2{}^{\bullet-} \longrightarrow Fe^{2+} + O_2$	$1.50 \times 10^{8}\,\mathrm{M^{-1}\,s^{-1}}$	Rush and Bielski (1985)
R14	$FeOH^{2+} + HO_2{}^\bullet \longrightarrow Fe^{2+} + O_2 + H_2O$	$1.30 \times 10^{5}\,\mathrm{M^{-1}\,s^{-1}}$	Ziajka et al. (1994)
R15	$FeOH^{2+} + O_2{}^{\bullet-} \longrightarrow Fe^{2+} + O_2 + HO^-$	$1.50 \times 10^{8}\,\mathrm{M^{-1}\,s^{-1}}$	Rush and Bielski (1985)
R16	$[FeOH_2]^+ + O_2{}^{\bullet-} \longrightarrow Fe^{2+} + O_2 + 2\,HO^-$	$1.50 \times 10^{8}\,\mathrm{M^{-1}\,s^{-1}}$	Rush and Bielski (1985)
	Fe(II)HCit Oxidant Reactions:		
R17	$FeC_6H_6O_7 + O_2^{\bullet-} \xrightarrow{H^+} FeC_6H_5O_7 + H_2O_2$	$6.00 \times 10^{5}\,\mathrm{M^{-1}\,s^{-1}}$	Pham and Waite (2008) (tuned)
R18	$FeC_6H_6O_7 + H_2O_2 \longrightarrow FeC_6H_5O_7 + H_2O + HO^\bullet$	$4.20 \times 10^{3}\,\mathrm{M^{-1}\,s^{-1}}$	Gonzalez et al. (2017)
R19	$FeC_6H_6O_7 + O_2 \longrightarrow FeC_6H_5O_7 + HO_2{}^\bullet$	$1.50\,\mathrm{M^{-1}\,s^{-1}}$	Gonzalez et al. (2017) (tuned)
R20	$FeC_6H_6O_7 + HO_2{}^\bullet \longrightarrow FeC_6H_5O_7 + O_2$	$4.20 \times 10^{5}\,\mathrm{M^{-1}\,s^{-1}}$	Pham and Waite (2008) (tuned)
	Organic/FeOH Photolysis:		
R21	$FeOH^{2+} \xrightarrow{h\nu} Fe^{2+} + HO^\bullet$	$4.51 \times 10^{-3}\,\mathrm{s^{-1}}$	Benkelberg and Warneck (1995)
R22	$[FeOH_2]^+ \xrightarrow{h\nu} Fe^{2+} + HO^\bullet + HO^-$	$5.77 \times 10^{-3}\,\mathrm{s^{-1}}$	Benkelberg and Warneck (1995)
R23	$C_5H_6O_5 \xrightarrow{h\nu} C_4 + CO_2$	$2.70 \times 10^{-5}\,\mathrm{s^{-1}}$	Dou et al. (2021)
R24	$C_4 \xrightarrow{h\nu} C_3 + CO_2$	$2.70 \times 10^{-5}\,\mathrm{s^{-1}}$	Dou et al. (2021)
R25	$C_5H_6O_5 \xrightarrow{h\nu} C_3 + 2\,CO_2$	$2.70 \times 10^{-6}\,\mathrm{s^{-1}}$	Dou et al. (2021)
R26	$C_5H_6O_5 \xrightarrow{h\nu} C_3 + C_2$	$2.70 \times 10^{-7}\,\mathrm{s^{-1}}$	Dou et al. (2021)
R27	$C_4 \xrightarrow{h\nu} C_2 + C_2$	$2.70 \times 10^{-6}\,\mathrm{s^{-1}}$	Dou et al. (2021)
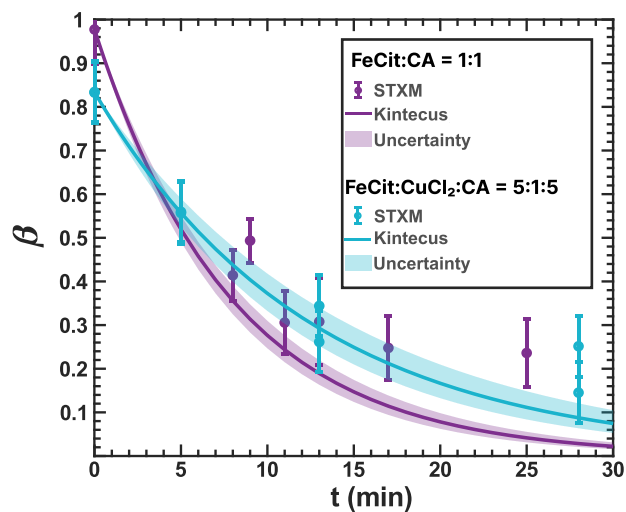
Figure 4. Iron(III) fraction, β, as a function of time irradiated with UV light from the LED with a narrow wavelength band centered at 370 nm. The plot shows circles and lines as measurements and model output, respectively. The light blue measurements, performed in the environmental cell without O_2 and RH = 0% show irradiation of $Fe^{III}(Cit):CuCl_2:CA$ at a $1:0.2:1$ mole ratio with the corresponding model output from this work. We have used UV intensity of $(2.36 \pm 0.06)\,W\,m^{-2}$, which resulted in a calculated photolysis frequency of $j = (1.4 \pm 0.2) \times 10^{-3}\,s^{-1}$ for 10 min. Violet data and model output are from a previous study using $Fe^{III}(Cit)/CA$ $(3.6 \pm 0.6)\,W\,m^{-2}$, and modeled using a photolysis frequency, $j = (2.20 \pm 0.04) \times 10^{-3}\,s^{-1}$ (Dou et al., 2021). An iron(II) quantum yield, $\phi = 1$, was used to calculate j. Error bars are $\pm\,0.07$ or propagated from the photon counting error, whichever is larger.

here), such photochemical enhancement may account for the higher ϕ in our reduction experiments compared to aqueous solutions.

3.2 Iron reoxidation experiments

Figure 5 shows STXM/NEXAFS images of $Fe^{III}(Cit)/CA$ particles from previous experiments (Alpert et al., 2021) (Figures 5a

245 and b), compared to images of $Fe^{III}(Cit)/Cu^{II}(Cit)/CA$ acquired in this study (Figures 5c and d), before and after reoxidation. The color bar indicates β determined from the STXM/NEXAFS experiments. Figure 5a was acquired after 10 min of illumination followed by ~ 2 min of reoxidation in the dark at 47% RH. In this case, the smaller particles and the outermost layers of the larger particles were more oxidized compared to the centers of the larger particles. Figure 5b is a STXM image of particles on the same sample one hour after the light was turned off, still showing only a small overall increase of the Fe^{III} fraction , and

250 again, more so in the outermost layers. As discussed in our previous work (Alpert et al., 2021), at this RH, this slow reoxidation is strongly limited by the supply of O_2, which fuels the formation of peroxy radicals that drives the process. Due to the short reacto-diffusive length for O_2 at this RH, this reaction occurred within a depth of just tens of nanometers, and the diffusional exchange of Fe^{II} and Fe^{III} between the bulk and the surface was slow (Alpert et al., 2021). When $Fe^{III}(Cit):Cu^{II}(HCit):CA$
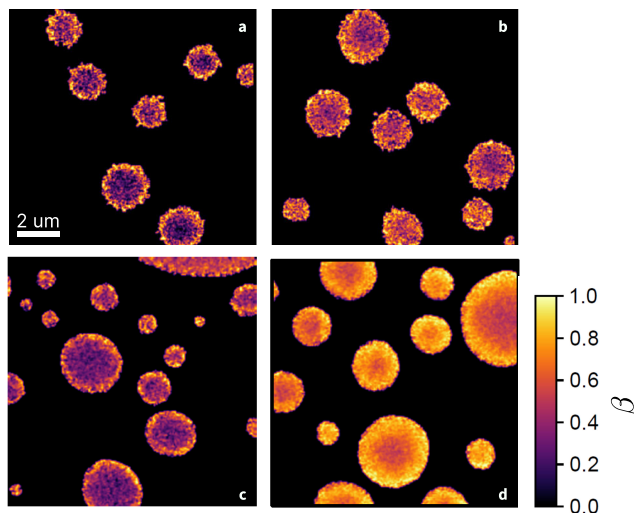
Figure 5. STXM/NEXAFS images of the iron(III) fraction, β, of **a** and **b** Fe^{III}(Cit):CA particles with a mole ratio of 1:1 shortly after irradiation and following more than three hours of reoxidation, respectively (adapted from Alpert et al. (2021) with permission by CC-BY license). **c** and **d**: Fe^{III}(Cit):Cu^{II}(Cit):CA particles with a mole ratio of 1:0.02:1 after being UV-aged for 10 min following $\sim$ 2 min and one hour of reoxidation, respectively. All images were taken under the same flow cell conditions at RH = 47% and $T = 20°C$.

particles were used with a mole ratio of 1:0.02:1 (Figures 5c and d), at the same RH, the initial photochemical reduction was similar, with a strong reduction in the particle centers and more oxidized surface layers. However, after 1 h dark reoxidation (Figure 5d), still at 47% RH, the particles showed a substantially greater extent of reoxidation compared to Figure 5b (after 3 h in the dark), with a several hundred nm thick Fe^{III} layer, a gradient in β towards the center of the particles and significantly higher Fe^{III} fraction throughout the particle.

The radial profile of β as a function of pixels and distance from the perimeter and the reoxidation time, t, is explored in Figure 6. This figure presents β from 1 to 35 pixels, or 35 nm to 1085 nm) from the perimeter of Fe^{III}(Cit):Cu^{II}(HCit):CA particles (mole ratio of 1:0.2:1) under RH = 47% and O$_2$, without prior irradiation. The color scale corresponds to the time since O$_2$ was introduced to the gas flow. Initial β values of the Fe^{III}(Cit)/Cu^{II}(HCit)/CA samples were in the same range of 0.8-1 as the data of Fe^{III}(Cit)/CA samples published in Alpert et al. (2021) and Dou et al. (2021). As a function of O$_2$ exposure without light, β remained constant throughout the experiment at $\sim$ 0.85 within error. Only at $t > 200$ min, iron(III) was slightly reduced in the center of the particles and oxidized in the outer shells. This experiment has shown that O$_2$ alone does not cause iron(III) to get significantly reduced or oxidized. The small fraction of Fe^{II} was initially likely due to handling, transferring and mounting the samples in the STXM environmental cell despite all efforts to keep them from exposure to ambient light (see Section 2.3).

In a new experiment (shown in Figure 7a), Fe^{III}(Cit)/Cu^{II}(HCit)/CA particles were irradiated for 10 min at low UV intensity, (2.36 ± 0.06) W m^{-2}, at the same RH = 47% as in Figure 6. A reduction in iron(III) was observed from $\beta = 0.9$ to 0.7 in the
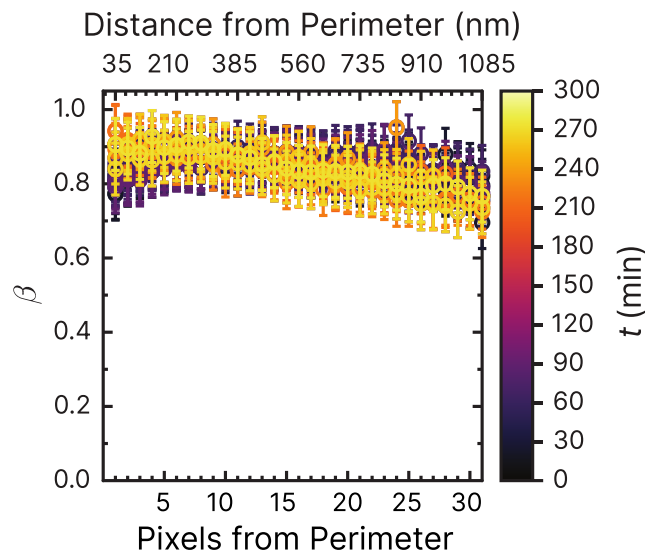
Figure 6. Iron(III) fraction, β, as a function of the distance and pixels from the perimeter of particles. Each line of data points corresponds to measurements of a single image of multiple particles at a given time, t, during O_2. The color scale is the t after O_2 was introduced to environmental cell. The experiment was conducted at RH = 47% with a mole ratio of $Fe^{III}(Cit) : Cu^{II}(HCit) : CA = 1 : 0.2 : 1$. Error bars are $\pm$ 0.07 or propagated from the photon counting error, whichever is larger.

interior of the particles within the first $30\,\text{min}$ (black dots), followed by slow reoxidization. In particular, no changes were detected on the perimeter of the particles (pixels from perimeter < 10). This contrasts with a previous study without copper (Alpert et al., 2021), where $Fe^{III}(Cit)/CA$ particles exposed to similar UV intensity ($(3.60 \pm 0.06)\,\text{W m}^{-2}$) and humidity (RH = 50%) showed markedly lower β. In that case, the initial reduction was also much more significant ($\beta \simeq 0.2$), and reoxidation occurred only slightly toward the surface. These findings indicate that copper strongly influences iron(III) reoxidation by altering the rate of Fe^{III} photoreduction (R1 in Table 3), despite the comparable photoreduction observed under vacuum conditions (Figure 4).

The measurement was repeated at a higher UV intensity ($(13.55 \pm 0.06)\,\text{W m}^{-2}$, as shown in Figure 7b). In this case, β remained high near the surface, but decreased sharply toward the center of the particles at values $\simeq 0.4 - 0.3$. Immediate after UV lights were turned off (early reoxidation, t= 0-15 min), β in the first $100\,\text{nm}$ dropped from about 0.8 to 0.7, while β dropped to 0.3 at $500\,\text{nm}$ within particles. We note that β reached values of 0.2 in the core of $Fe^{III}(Cit)/CA$ particles within the first $100\,\text{nm}$ from the perimeter of particles (Alpert et al., 2021), in stark contrast to our observations where much higher light intensity was used. Experiments under different humidity conditions allow us to further differentiate the impact of copper on ϕ and the reoxidation rate.

Figure 8 shows experiments at RH = 60%, using the same mole ratios of $Fe^{III}(Cit)/Cu^{II}(HCit)/CA$ particles and irradiation conditions as in Figure 7b. In Figure 8a, iron was seeming reoxidized immediately after being reduced. Our first measurement at $t \approx 10\,\text{min}$ (black dots) after light was switched off, iron was slightly reduced compared to the initial fraction in grey. This
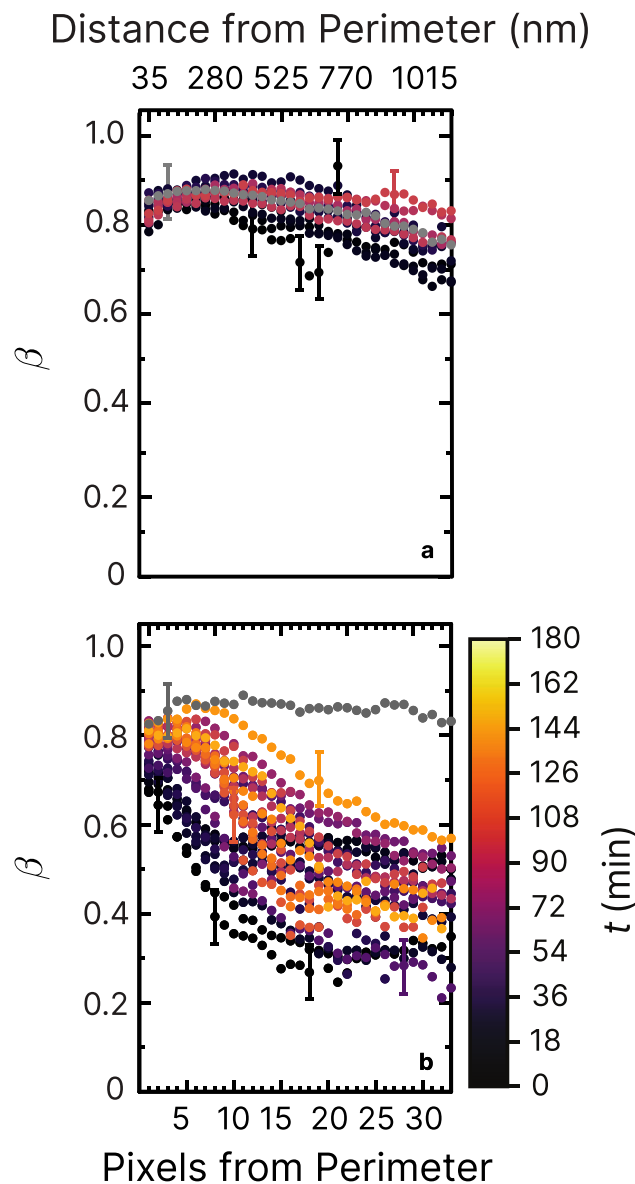
Figure 7. Iron(III) fraction, β, as a function of the distance and pixels from the perimeter of particles and time, t, after UV light was switched off at RH = 47% and a $Fe^{III}(Cit):Cu^{II}(HCit):CA$ mole ratio of $1:0.2:1$. The particles were irradiated after measuring the initial fraction β before irradiation (gray dots). The UV intensity used was **a** $(2.36 \pm 0.06)\,W\,m^{-2}$ and **b** $(13.55 \pm 0.06)\,W\,m^{-2}$ resulting in a calculated photolysis frequency of $j = (1.4 \pm 0.2) \times 10^{-3}\,s^{-1}$ for 10 min and in **b** $j = (8.1 \pm 0.2) \times 10^{-3}\,s^{-1}$ for 10 min. The iron(III) fraction was then measured until $\approx 150\,min$ after irradiation (light orange dots). The error bars are not shown for better visibility, but similar in magnitude to Figure 6. Error bars are $\pm\,0.07$ or propagated from the photon counting error, whichever is larger.
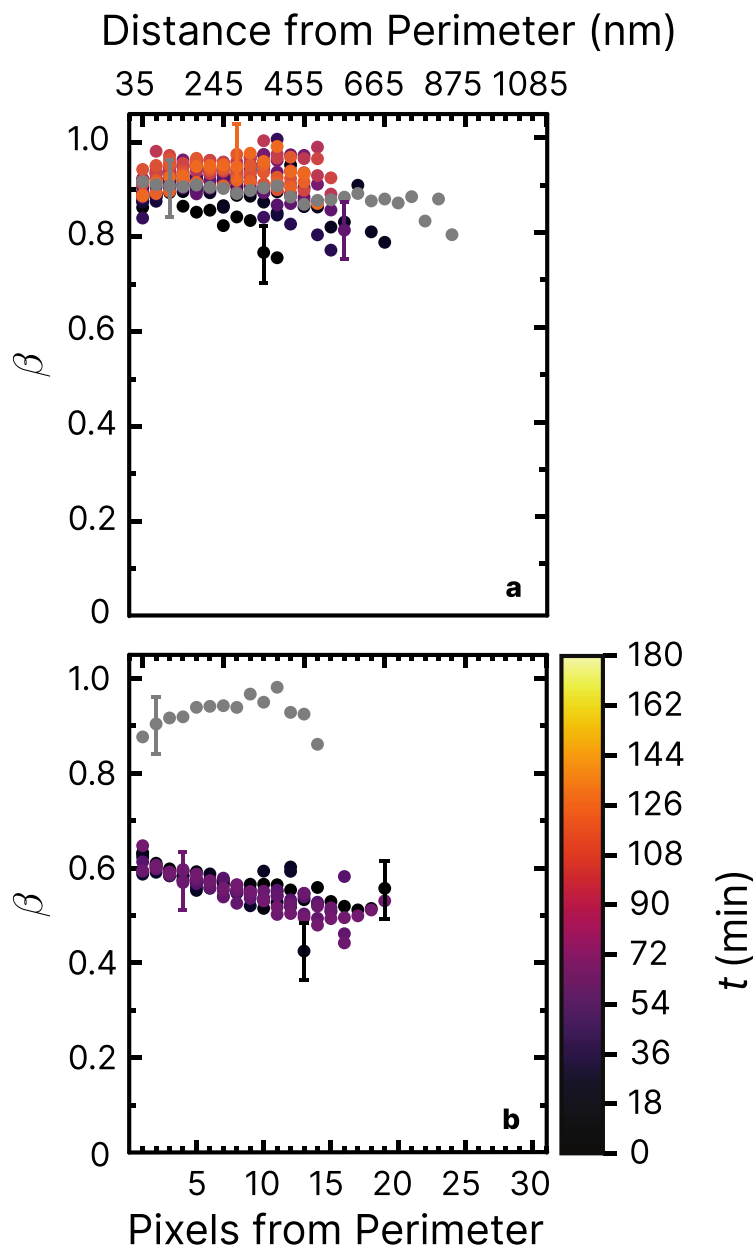
Figure 8. Iron(III) fraction, β, as a function of the distance and pixels from the perimeter of particles and time, t, after UV light was switched off at RH = 60% and a $Fe^{III}(Cit):Cu^{II}(HCit):CA$ mole ratio of $1:0.2:1$ with a UV intensity of $(13.55\pm0.06)\,\mathrm{W\,m^{-2}}$ resulting in a photolysis frequency of $j = (8.1\pm0.2)\times10^{-3}\,\mathrm{s^{-1}}$. **a**: oxygen was present in the environmental cell (see Fig. 2), whereas in **b** only helium was present. Error bars are ± 0.07 or propagated from the photon counting error, whichever is larger.
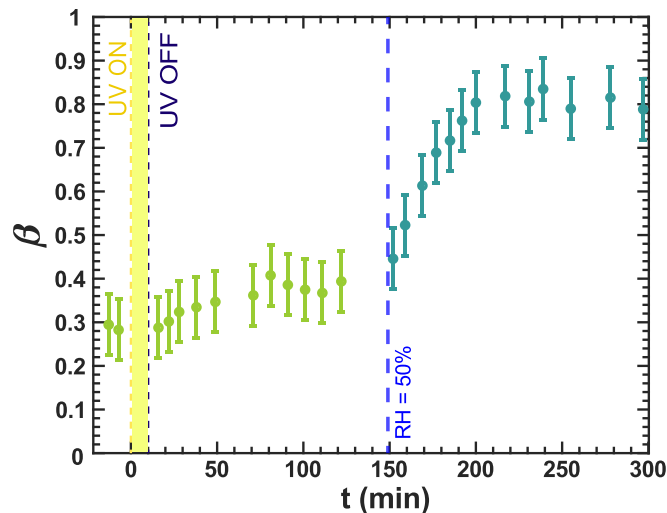
Figure 9. Iron(III) fraction, β, as a function of time, t, in a specifc experiment for irradiation at t = 0-10 min at a UV intensity of $(13.55 \pm 0.06)\,\mathrm{W\,m^{-2}}$ resulting in a photolysis frequency of $j = (8.1 \pm 0.2) \times 10^{-3}\,\mathrm{s^{-1}}$ and RH = 20% with a mole ratio of $\mathrm{Fe^{III}(Cit)}$: $\mathrm{Cu^{II}(HCit)}$: CA = 1 : 0.2 : 1. The first data points at $t < 0$ denote the initial β before irradiation. At t = 149 min, RH was increased to 50%. Note that this experiment was conducted after the experiments in Figure 7, where irradiation occurred previously for 10 min. Error bars are $\pm$ 0.07 or propagated from the photon counting error, whichever is larger.

contrasts with the reduction observed in Figure 7b. We suggest two possibilities to explain this, one being that $\mathrm{Fe^{III}(Cit)}$ was not photolyzed as efficiently in the presence of copper at RH = 60%, which would mean that ϕ would decrease with increasing

290 RH. Another is that copper causes a faster reoxidation, that are comparable to the time it takes to acquire the first images after switching off light. In the experiment shown in Figure 8b, $\mathrm{Fe^{III}(Cit)/Cu^{II}(HCit)/CA}$ particles were again irradiated at RH = 60%, but without O_2. We observed iron was indeed reduced, reaching $\beta = 0.5$. However, this was as not even as much as was the case for $\mathrm{Fe^{III}(Cit)/CA}$ samples at RH = 40% with oxygen found to be reduced to a lower value of $\beta = 0.2$ in Alpert et al. (2021). No reoxidation was detected in Figure 8b, as we observed β remained low for an hour. We conclude that both a low ϕ

295 for iron(III) reduction (compared with $\mathrm{Fe^{III}(Cit)}$ without copper), but also faster reoxidation in presence of copper (and O_2) is the reason for the observations. Experiments of $\mathrm{Fe^{III}(Cit)/Cu^{II}(HCit)/CA}$ particles containing ten times less copper (mole ratio of 1 : 0.02 : 1) are shown in the SI Figure D1, and aligns well with previous results of $\mathrm{Fe^{III}(Cit)/CA}$ (Alpert et al., 2021) and our results of $\mathrm{Fe^{III}(Cit)/Cu^{II}(HCit)/CA}$ 1 : 0.2 : 1 shown in Figure 7 and 8. The trend of β in experiments with O_2 at RH = 20% (Figure D2) is similar to that at RH = 60% without O_2. Iron in the particles did not reoxidize at all (β = 0.45 after $t \simeq 10\,\mathrm{h}$).

300 Thus, reoxidation here was clearly limited by the oxygen supply to the particles, probably due to diffusion limitations at high viscosity, and the initial reduction in presence of copper was less than for $\mathrm{Fe^{III}(Cit)/CA}$.

We also assessed the impact of RH on iron reoxidation through a dynamic experiment in which RH was increased during a dark reoxidation period. In Figure 9, the iron(III) fraction averaged over 10 to 15 particles in an image is plotted as a function

of t, whereas in Figure 7 the position-dependent iron(III) fractions are shown. Initially, at 20%, no reoxidation was observed, consistent with the spatially resolved images in Figure D2. At $t = 149$ min RH was raised to 50% and β immediately began to increase, reaching 0.8 at approximately 198 min. This reoxidation for 49 min was much faster than in the experiment where UV irradiation occurred at RH = 47% (see Figure 7b). Reoxidation intensified with an increase in RH, allowing O_2 to diffuse into the particle phase, as discussed in Alpert et al. (2021) and in Figures 7 and 8. Thus diffusion limitations leading to anoxic conditions (Alpert et al., 2021) also explain our observations with $Fe^{III}(Cit)/Cu^{II}(HCit)/CA$ particles.

3.3 Copper containing samples revealed lower iron(II) quantum yield of $Fe^{III}(Cit)$ photochemistry

The experimentally observed changes in the reoxidation of iron(II) to iron(III) in presence of copper call for a reassessment of the $Fe^{III}(Cit)$ photochemical system both with and without copper. We aim to elucidate the role of copper in $Fe^{III}(Cit)$ photochemistry by adapting and extending the mechanism for the box model calculations. The experiment in Figure 4 provides evidence for an iron(II) quantum yield, $\phi = 1$ for solid $Fe^{III}(Cit)$ in vacuum, and this high $\phi = 1$ was then also used to explain the reoxidation data in Figure 3, to reproduce the simulation results with the depth resolving model in our previous work (Dou et al., 2021), as a sanity check of the present homogeneous box model. As mentioned in the introduction, a number of previous studies investigating the photochemistry of different aqueous iron(III) polycarboxylate complexes, including $Fe^{III}(Cit)$, reported lower ϕ in the range of 0.1 - 0.4 and its sensitivity to O_2 (Faust and Zepp, 1993; Glebov et al., 2011; Pozdnyakov et al., 2014; Abrahamson et al., 1994; Pozdnyakov et al., 2012; Weller et al., 2013). The presence of dimeric or polymeric complexes, formed through paramagnetic coupling among Fe centers via oxygen bridges, seems crucial for both absorbance and ϕ. These complexes also influence photochemical outcomes, as the reduced radical complex can interact with a remaining Fe(III) center of the same dimer (Abrahamson et al., 1994; Glebov et al., 2011; Pozdnyakov et al., 2014).

Our model, simulating the reoxidation experiment at a RH = 40%, is closely aligned with the experimental results shown in Figure 3. In turn, for the higher RH, the simulated iron(III) fractions drop more strongly initially than what the data seem to indicate. This indicates that ϕ may be influenced by the phase state of the particles. For very high viscosity, thus for the vacuum conditions, the Fe^{II} radical complex may get frozen, justifying the high $\phi = 1$. For RH = 40% we adjusted ϕ to 0.9, and for experiments at higher humidity (RH = 50 and 60%) and lower viscosities, we allowed ϕ to have a lower value to represent a transition from high ϕ at low RH to ϕ values found in previous studies in aqueous environment. We found that a value of 0.5 led to a better fit of the data for the two higher RH conditions than when applying $\phi = 1$, as shown in Figure 10. As mentioned above, this sensitivity of ϕ to the water activity and thus to the solute concentration could result from the polynuclear complexes that likely change in abundance in parallel.

Based on the experimental results presented above, copper's effect is evident in two ways. First, ϕ at RH $\geq$ 20% is substantially lower compared to $Fe^{III}(Cit)$ alone. Second, reoxidation is accelerated in the presence of copper, resulting in near-complete reoxidation shortly after UV light was switched off. Our box model permits changing ϕ with Cu content and incorporates known reactions between Cu and Fe, as well as Cu and ROS species. This extended box model will be used to fit the STXM/NEXAFS $Fe^{III}(Cit)/Cu^{II}(HCit)/CA$ UV-aging experiments. Several studies have proposed iron-copper mechanisms for carboxylic acid systems similar to CA (Ervens et al., 2003; Mao et al., 2013; Weller et al., 2014; Shen et al., 2021; Gonzalez
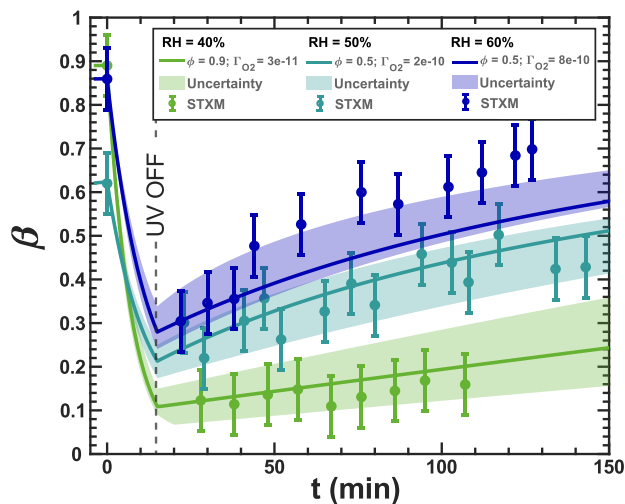
Figure 10. The data in Figure 3 is shown and compared with model scenarios with oxygen uptake coefficient, Γ_{O_2}, and quantum yield, ϕ, shown as different colors (green: RH = 40% with $\phi = 0.9$ and $\Gamma_{O_2} = (3 \pm 2) \times 10^{-11}$; turquoise: RH = 50% with $\phi = 0.5$ and $\Gamma_{O_2} = (2 \pm 1) \times 10^{-10}$; blue: RH = 60% with $\phi = 0.5$ and $\Gamma_{O_2} = (8 \pm 6) \times 10^{-10}$). Model uncertainties are defined as in Figure 3.

Table 4. Copper equilibria written as forward and back reactions with their rate constants.

Nr.	Equilibria	k_r	K_{eq}	References
E15	$Cu^{2+} + C_6H_5O_7^{3-} + H^+ \longrightarrow CuC_6H_6O_7$	$1.00 \times 10^{10}\,M^{-1}\,s^{-1}$	$4.79 \times 10^8\,M^{-1}$	Perrin (1979)
E15b	$CuC_6H_6O_7 \longrightarrow Cu^{2+} + C_6H_5O_7^{3-} + H^+$	$20.9\,s^{-1}$		
E16	$Cu^{2+} + C_6H_5O_7^{3-} + 2H^+ \longrightarrow CuC_6H_7O_7^+$	$1.00 \times 10^{10}\,M^{-1}\,s^{-1}$	$2.19 \times 10^{11}\,M^{-1}$	Perrin (1979)
E16b	$CuC_6H_7O_7^+ \longrightarrow Cu^{2+} + C_6H_5O_7^{3-} + 2H^+$	$4.57 \times 10^{-2}\,s^{-1}$		

et al., 2017). We integrated the relevant chemistry into the fundamental Fe^{III}(Cit)/CA mechanism (see Section 2.5). The resulting copper equilibria and reactions, along with their corresponding rate constants, are listed in Tables 4 and 5, and were added to the existing chemical mechanism (Tables 1, 2 and 3) in Kintecus. To the best of our knowledge we believe that our model thus incorporates the important reactions potentially relevant to assess the role of copper in our system.

Determining the iron(II) quantum yield (ϕ) to accurately simulate the Fe^{III}(Cit)/Cu^{II}(HCit)/CA experiments required conducting a reoxidation experiment in the absence of oxygen. At RH = 60% and a light intensity of $(13.55 \pm 0.06)\,W\,m^{-2}$, we observed and simulated the initial reduction of iron(III) in the Fe^{III}(Cit)/Cu^{II}(HCit)/CA system. Figure 11 shows the results of an optimization run, where j was calculated to $(8.1 \pm 1.0) \times 10^{-4}\,s^{-1}$ using $\phi = 0.1$. In this case, oxygen-related iron(II)

Table 5. Copper, ROS, and Cu-Fe coupling reactions with their reaction rate constants at a constant pH = 2.

Number	Reactions	k_r	References
	ROS Reactions:		
R28	$Cu^+ + HO^{\bullet} \longrightarrow Cu^{2+} + HO^-$	$3.00 \times 10^9\,M^{-1}\,s^{-1}$	Goldstein et al. (1992)
R29	$Cu^+ + O_2 \longrightarrow Cu^{2+} + O_2^{\bullet-}$	$4.60 \times 10^5\,M^{-1}\,s^{-1}$	Bjergbakke et al. (1976)
R30	$Cu^+ + H_2O_2 \longrightarrow Cu^{2+} + HO^{\bullet} + HO^-$	$7.00 \times 10^3\,M^{-1}\,s^{-1}$	Berdnikov (1973)
R31	$Cu^+ + HO_2^{\bullet} \xrightarrow{H^+} Cu^{2+} + H_2O_2$	$3.50 \times 10^9\,M^{-1}\,s^{-1}$	Berdnikov (1973)
R32	$Cu^+ + O_2^{\bullet-} \xrightarrow{2H^+} Cu^{2+} + H_2O_2$	$9.40 \times 10^9\,M^{-1}\,s^{-1}$	von Piechowski et al. (1993)
R33	$Cu^{2+} + HO_2^{\bullet} \longrightarrow Cu^+ + O_2 + H^+$	$1.00 \times 10^8\,M^{-1}\,s^{-1}$	Rabani et al. (1973)
R34	$Cu^{2+} + O_2^{\bullet-} \longrightarrow Cu^+ + O_2$	$8.00 \times 10^9\,M^{-1}\,s^{-1}$	Rabani et al. (1973)
	Cu-Fe Coupling:		
R35	$Fe^{3+} + Cu^+ \longrightarrow Cu^{2+} + Fe^{2+}$	$1.30 \times 10^7\,M^{-1}\,s^{-1}$	Bjergbakke et al. (1976)
R36	$FeOH^{2+} + Cu^+ \longrightarrow Cu^{2+} + Fe^{2+} + HO^-$	$1.30 \times 10^7\,M^{-1}\,s^{-1}$	Sedlak and Hoigné (1993)
R37	$[FeOH_2]^+ + Cu^+ \longrightarrow Cu^{2+} + Fe^{2+} + 2\,HO^-$	$1.30 \times 10^7\,M^{-1}\,s^{-1}$	Mao et al. (2013)

reoxidation was excluded, enabling a simulation solely driven by copper and/or inhibited iron(III) reduction. It is important to note that these STXM/NEXAFS data correspond to those shown in Figure 8b, but are averaged at a single time step. We propose that $\phi_{Fe^{III}(Cit)/Cu^{II}(HCit)/CA} \ll \phi_{Fe^{III}(Cit)/CA}$ by a factor of 5. Given the sensitivity of $\phi = 0.1$ to the presence of polynuclear iron complexes, we speculate that it results from copper replacing an iron center in a polynuclear complex or from copper
350   inhibiting the secondary reaction of the reduced radical complex with $Fe^{III}(Cit)$ in a catalytic way.

    We present the optimized simulation results for different $Fe^{III}(Cit)/Cu^{II}(HCit)/CA$ reoxidation experiments conducted under various mole ratios, RH conditions and using $\phi = 0.1$ shown in Figures 12 and 13. At RH = 20% in Figure 12, the reduction occurred while the UV lights were on. After turning them off, we observed no reoxidation, as expected, and the particles were likely highly viscous and therefore lacked the sufficient oxygen supply needed for reoxidation, similar to the observations
355   in Figure 11. The model is in excellent agreement with the observations considering the experimental uncertainty. At RH = 47%, reoxidation after UV lights were switched off was consistent and significant, increasing from approximately $\beta = 0.4$ to 0.8 from t = 10-200 min. The increased molecular diffusion at this higher RH likely accounts for the greater reoxidation compared to RH=20%. However, there is some data scatter, especially for t = 10-40 min, which we suggest indicates fast reoxidation occurring on a time scale comparable to the acquisition of STXM/NEXAFS images, even under UV irradiation
360   ($t < 10$ min). In particular, our model captures all the experimental data, taking into account both the model and experimental uncertainties resulting from the measurement error of RH and the light intensity, as well as the error in Γ_{O_2}. The width of the uncertainty of the model is much larger than that of other RH in Figure 12, indicating that the photochemical reduction and dark reoxidation rates are highly sensitive at RH = 47%. At RH = 60%, reduction was not observed with $\beta > 0.85$ observed throughout the experiment, possibly due to reoxidation that occurs on short time scales that we could not experimentally
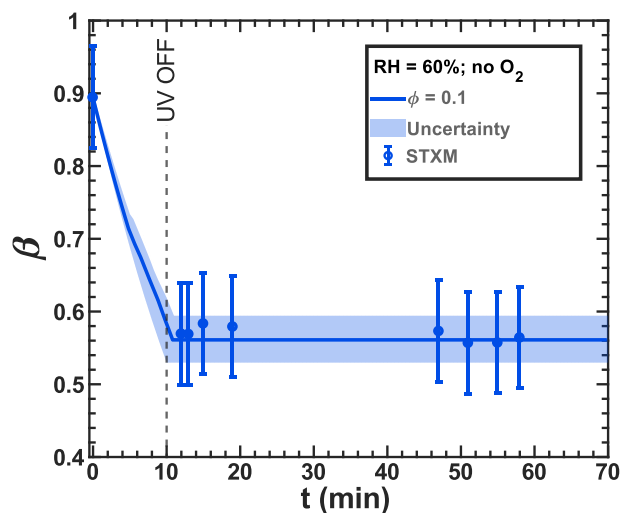
Figure 11. Iron(III) fraction, β, as a function of time, t, for irradiation at $t = 0\text{-}10\,\text{min}$ with a light intensity of $(13.55 \pm 0.06)\,\text{W}\,\text{m}^{-2}$ and RH = 60% with a mole ratio of $\text{Fe}^{\text{III}}(\text{Cit}):\text{Cu}^{\text{II}}(\text{HCit}):\text{CA} = 1:0.02:1$ and without oxygen in the gas phase. The circles with error bars represent the average of all particles mapped in one time step during the STXM experiments (data of Figure 8b). Data uncertainty (error bars), model prediction and model uncertainties (straight lines and shading, respectively) are as defined in Figure 3. The iron(II) quantum yield, $\phi = 0.1$, was fit to the STXM/NEXAFS data and used to derive the photolysis frequency, $j = (8.1 \pm 1.0) \times 10^{-4}\,\text{s}^{-1}$ used in the model.

resolve ($< 2\,\text{min}$). Despite using $\Gamma_{\text{O}_2} = 1 \times 10^{-8}$, which corresponds to well-mixed conditions in the aqueous phase without any diffusion limitations, our model could not reproduce this fast reoxidation. We proof such a diffusion limitation by deriving the reacto-diffusive length of oxygen in the SI (Section G2) resulting in $5.3\,\text{nm}$. This implies that even at high RH of 65%, the limitation by reaction and diffusion is crucial for the O_2 uptake

   Figure 13 shows experimental and modeling results for a copper content reduced by a factor of ten compared to Figure 12. At RH = 47%, we again observed a reduction during irradiation by UV light and reoxidation in the dark after UV light was switched off. Our model is in agreement with the observations, which were toward the top of the green-shaded area, indicating the model uncertainty. Unlike Figure 12, there was very little data scatter in the 30 min after UV light was switched off. At RH = 60%, we observed some reduction and reoxidation, in contrast to Figure 12. Although the data tend to scatter more for this experiment, there was a clear drop of β, from 0.8 initially to 0.6, followed by reoxidation to a maximum of 0.86 at $t = 92\,\text{min}$. Our model could not capture the reduction by UV light and predicted a slower reoxidation for lower copper content. Interestingly, in Figure 13, $\beta > 0.8$ was not reached by our model and occurred only at the last data point, while this was easily observed in Figure 12 at the same RH. We also emphasize that our model does not explicitly include other HO_2 formation pathway such as photolysis of C_5 ketone products other than elimination of HO_2 from the citrate peroxy radical, which could cause an uncertainty about the true HO_2 and H_2O_2 production. For this, the model had been optimized to fit the available observables. From all of these observations and the fact that we have included all relevant reactions involving copper in our
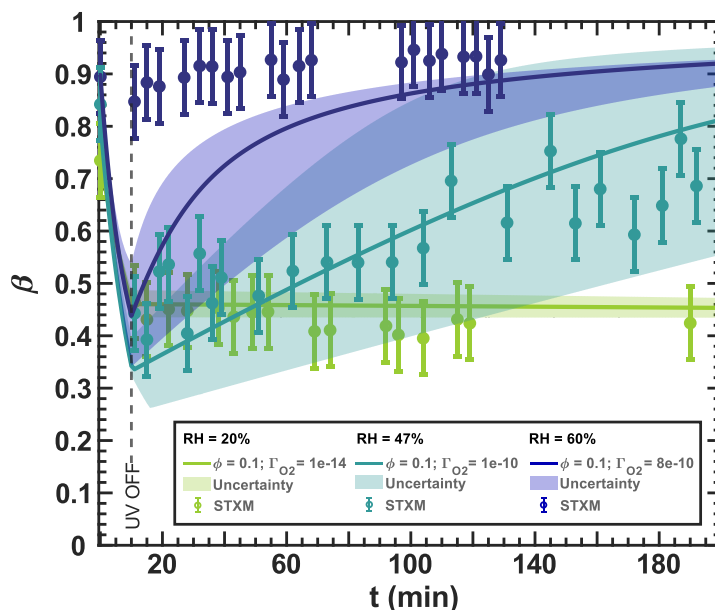
Figure 12. Iron(III) fraction, β, as a function of time, t, for irradiation at $t = 0\text{-}10\,\text{min}$ with a light intensity of $(13.55 \pm 0.06)\,\text{W}\,\text{m}^{-2}$, RH = 60% (blue), 47% (turquoise) and 20% (green) with a mole ratio of $\text{Fe}^{\text{III}}(\text{Cit}):\text{Cu}^{\text{II}}(\text{HCit}):\text{CA} = 1:0.2:1$. The circles with error bars represent the average of all particles mapped in one time step during the STXM experiments. Data uncertainty (error bars), model prediction and model uncertainties (straight lines and shading, respectively) are as defined in Figure 3. The iron(II) quantum yield, $\phi=0.1$, was taken from the anoxic experiment shown in Figure 11, which resulted in a photolysis frequency of $j = (8.1 \pm 1.0) \times 10^{-4}\,\text{s}^{-1}$). Oxygen uptake coefficients, Γ_{O_2}, are indicated in the legend.

box model, we suspect that a missing iron(II) reoxidation pathway exists during UV irradiation and/or during dark periods that are related to copper increasing a chemical reoxidation pathway.

3.4 Copper(II) oxidizing Iron(II)?

Observed reoxidation during UV irradiation and after UV light was turned off ($t = 0 - 40\,\text{min}$) at RH = 47 and 60% (Figures 12 and 13) was underestimated. To elucidate the reasons, we derived turnover rates (d[reaction]/dt) to identify the main chemical reactions responsible for both $\text{Fe}^{\text{III}}(\text{Cit}):\text{CA}$ and $\text{Fe}^{\text{III}}(\text{Cit}):\text{Cu}^{\text{II}}(\text{Cit}):\text{CA}$ experiments. We selected experiments carried out at RH = 60%, where transport limitations may play a lesser role. Figures 14 and 15 show turnover rates of the $\text{Fe}^{\text{III}}(\text{Cit}):\text{Cu}^{\text{II}}(\text{HCit}):\text{CA} = 1:0.2:1$ (RH = 60%) experiment from Table 3 ($\text{Fe}^{2+}/\text{Fe}^{\text{II}}(\text{HCit})$ oxidant reactions) and Table 5 (Cu-ROS and Cu-Fe coupling reactions), respectively. In the basic $\text{Fe}^{\text{III}}(\text{Cit})$ photochemical system (Table 3) the two dominating reactions that oxidize iron(II) to iron(III) are R19 and R20 (green and light blue in Figure 14) with turnover rates of $\approx 10 \times 10^{-3}\,\text{M}\,\text{s}^{-1}$. In these reactions, both O_2 and HO_2 act as oxidants. In the case of $\text{Fe}^{\text{III}}(\text{Cit}):\text{CA}$ (RH = 60%) experiment simulation (see Figure F1), HO_2 is the predominant oxidant, with R20 occurring at a similarly fast rate in presence of copper. Oxidation with
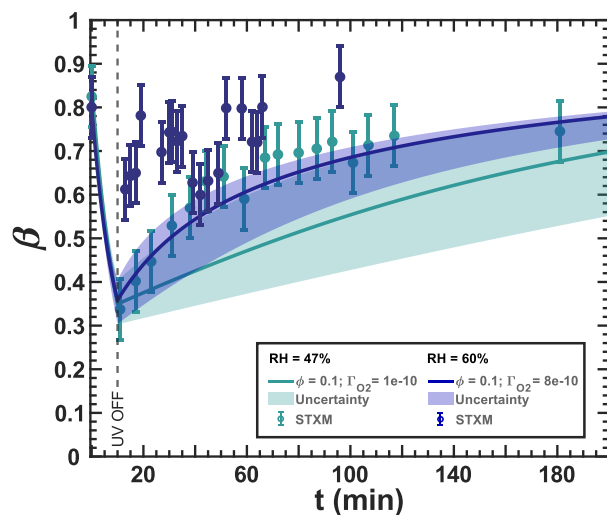
Figure 13. Iron(III) fraction, β, as a function of time, t, for irradiation at $t = 0\text{-}10$ min with a light intensity of $(13.55 \pm 0.06)\,\mathrm{W\,m^{-2}}$, RH $= 60\%$ (blue) and 47% (turquoise) with a mole ratio of $Fe^{III}(Cit):Cu^{II}(HCit):CA = 1:0.02:1$ (ten times less copper than in Figure 12). The circles with error bars represent the average of all particles mapped in one time step during the STXM experiments. Data uncertainty (error bars), model prediction and model uncertainties (straight lines and shading, respectively) are as defined in Figure 3. The iron(II) quantum yield, $\phi=0.1$, was taken from the anoxic experiment shown in Figure 11, which resulted in a photolysis frequency of $j = (8.1 \pm 1.0) \times 10^{-4}\,\mathrm{s^{-1}}$). Oxygen uptake coefficients, Γ_{O_2}, are indicated in the legend.
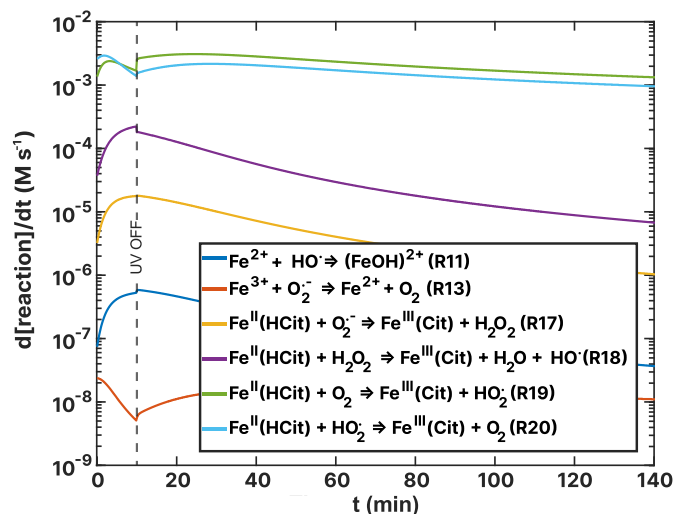
Figure 14. Turnover rates (d[reaction]/dt) of $Fe^{II}(HCit)$ and $Fe^{2+}\text{-}Fe^{3+}$ ion loss reactions as a function of time, t, of the simulation of the $Fe^{III}(Cit):Cu^{II}(Cit):CA = 1:0.2:1$ (RH = 60%) experiment as listed in Table 3. UV radiation is turned off at $t = 10$ min.
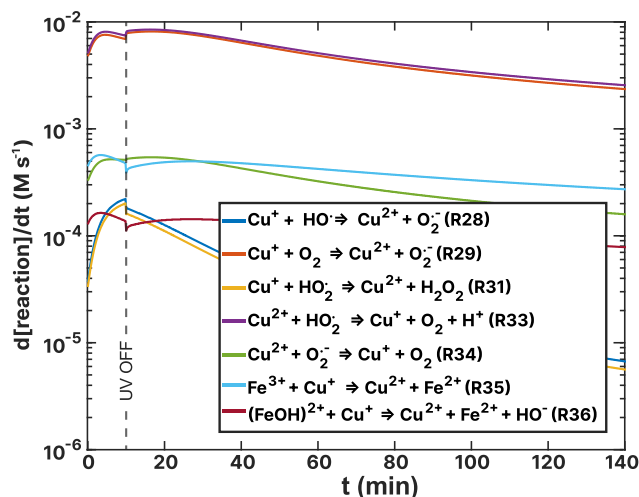
Figure 15. Turnover rates (d[reaction]/dt) of copper-ROS and Cu-Fe reoxidation reactions as a function of time, t, of the simulation of the $Fe^{III}(Cit):Cu^{II}(Cit):CA = 1:0.2:1$ (RH = 60%) experiment as listed in Table 5. UV radiation is turned off at $t = 10\,\text{min}$.

O_2 (R19) and H_2O_2 (R18) are one order of magnitude slower. In absence of copper, OH remains a significant oxidant (R11). These results suggest that variations in ROS concentration and turnover may provide insight to the observed discrepancies,
395 which we explore below.

Among the turnover rates shown in Figure 15 for copper redox reactions, R29 and R33 are the highest, reaching $10^{-2}\,\text{M s}^{-1}$. These reveal a steady-state of hydroperoxyl radicals, where copper is initially oxidized via R29 and then HO_2 reduces Cu^{2+} back to Cu^+. Notably, the only sink for hydroperoxyl radicals is the self-reaction R31 (yellow) with turnover rates between 10^{-5}-$10^{-4}\,\text{M s}^{-1}$ producing H_2O_2. The concentration of Cu^{2+} is sustained by Fe^{3+} reoxidation as visible in light blue (R35).
400 We interpret these reactions as the primary contributors to elevated hydrogen peroxide (H_2O_2) concentration in the model of $Fe^{III}(Cit):Cu^{II}(HCit):CA$ experiments. The ROS concentrations for both $Fe^{III}(Cit):CA$ and $Fe^{III}(Cit):Cu^{II}(HCit):CA$ experiments are compared in Figure F3 in the SI. In $Fe^{III}(Cit):Cu^{II}(HCit):CA$ experiments, H_2O_2 concentration is the highest among all ROS at $\approx 1 \times 10^{-8}\,\text{mol L}^{-1}$. This is in contrast to $Fe^{III}(Cit):CA$ samples, where the concentrations of OH and HO_2 are comparable to that of H_2O_2, differing no more than one order of magnitude. We attribute the elevated H_2O_2 concentration to
405 the reoxidation of Cu^+ by HO_2 in R31.

Examining the O_2 concentrations for both samples (see Figure F4 in the SI) and comparing them with the ROS concentrations previously discussed, we observed a mildly inverse trend across all concentrations. Specifically, during UV exposure, ROS concentrations gradually rise and then consistently decline after the light is turned off. In contrast, the O_2 concentrations drop significantly during UV exposure and gradually increase during the dark reoxidation phase. That suggests that under UV light,
410 ROS production is O_2 limited. However, in $Fe^{III}(Cit):Cu^{II}(HCit):CA$ samples, the higher O_2 concentration accelerates the $Fe^{II}(HCit)$ reoxidation (R19), which is buffered by Fe^{3+} reduction by Cu^+ in R35. The reduction of iron and the decreased

Table 6. Tuned redox reactions incorporated into the mechanism (Tables 3 and 5.)

Number	Reactions	k_r	References
	Cu(II) mediated Fe(II) reoxidation reactions		
R38	$CuC_6H_6O_7 + Fe^{2+} \xrightarrow{H^+} Fe^{3+} + CuC_6H_7O_7$	$9 \times 10^5 \ M^{-1}s{-}1$	tuned
R39	$Cu^{2+} + Fe^{2+} \longrightarrow Fe^{3+} + Cu^+$	$1 \times 10^9 \ M^{-1}s{-}1$	tuned

hydroperoxyl radical levels in the presence of copper may explain why increasing reaction rates for R19 and R20 did not alter the iron(II) reoxidation rate when attempting to fit the model to the experimental data. As a sanity check, we again increased the O_2 uptake coefficient to the level of well-mixed conditions, as it was done for the uncertainty limits above, to confirm that
415 O_2 flux into the condensed is not the sole driver of the fast reoxidation.

In conclusion, with existing chemical mechanisms found in the literature of dilute aqueous phase redox chemistry of iron and copper and optimizations of the corresponding rate constants, we could not simulate the observed change in reoxidation with copper at RH = 60%. Thus, we assert that a copper(II)-catalyzed reaction, which reoxidizes iron(II) during UV-aging, is essential for enhancing the model's performance. Although not thermodynamically favoured, Matocha et al. (2005) observed
420 a rapid reduction of Cu^{II} to Cu^I in the aqueous phase by dissolved Fe^{II} in the absence of oxygen, under conditions where precipitation of Cu(I) oxides or hydroxides prevented reoxidation by Fe(III). Also, reactions 38 and 39 may also occur in the same way for Fe(II) complexes, not explicitly added to our mechanism. Here, copper can replace one of the iron centers and behave in a similar way as in a solid mixed Fe-Cu-oxide, which effectively drives the redox equilibrium in the other direction as that expected for dilute aqueous solution of free metal ions and their complexes. Another study demonstrated synergies between
425 iron and copper oxides under oxygen rich conditions, suggesting the possibility of direct contact between Fe_2O_3 and CuO on the surface of a fly ash surrogate (Potter et al., 2018). D'Huysser et al. (1981) found similar conversion but also cautioned that they could be X-ray induced. Ammann et al. (1992) reported the conversion of mixed Cu(II)/Fe(II) into Cu(I)/Fe(III) in effloresced aerosol particles generated from mixed aqueous Cu(II)/Fe(II) chloride solutions. Additionally, Goh et al. (2006) suspected the presence of Cu(I) in chalcopyrite, indicating mixed Cu-Fe sulfides. This may suggest an interaction between copper and iron
430 ions in contact within mixed crystalline systems, where a different electrochemical equilibrium (favoring Cu(I)/Fe(III)) could occur, as opposed to aqueous solutions (favoring Cu(II)/Fe(II)). We hypothesize that similar coupling could take place in mixed Cu-Fe polynuclear citrate complexes. Based on this hypothesis, we included two direct reactions oxidizing Fe(II) to Fe(III) via reduction of Cu(II) to Cu(I). Although we did not explicitly model polynuclear complexes, we consider their reaction may aid in explaining our observations. The Cu^{2+} induced reoxidation reactions are listed in Table 6 (R38 and R39).
435 The new simulation of the $Fe^{III}(Cit):Cu^{II}(HCit):CA = 1:0.02:1$ experiments with RH = 60% incorporating R38 and R39 is shown in Figure 16. The blue data points are the same as those in Figure 13. (1 : 0.2 : 1 results in Figure G1 the SI). These reactions tend to reoxidize iron at the expense of reducing Cu and agree well with our data, largely by imposing a slightly lower O_2 transfer coefficient of $\Gamma_{O2} = 3.5 \times 10^{-10}$, instead of 8×10^{-10} from Figures 12 and 13). Iron reoxidation was well represented $30 \, min$ after the UV light was turned off. Interestingly, the simulation exhibited transient intermediate behavior
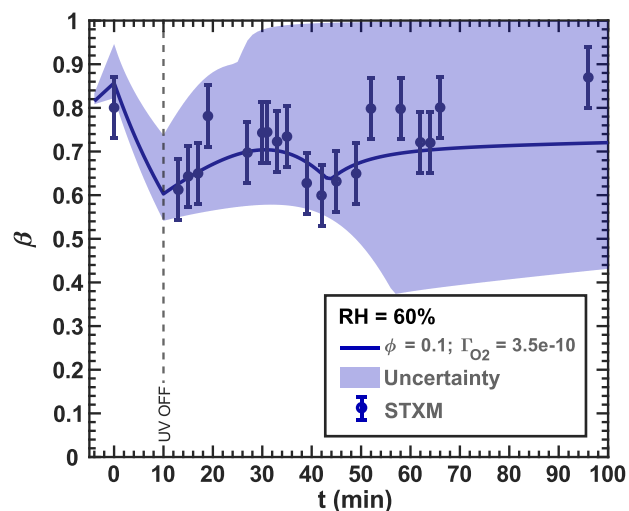
Figure 16. Data reproduced from Figure 13. The O_2 uptake coefficient of the RH =60% model run ($\Gamma_{O_2}(60\%RH)$ was slightly adjusted from 8×10^{-10} from the initial Fe^{III}(Cit)/CA mechanism to 3.5×10^{-10}. The lower and upper boundary of the model uncertainty (blue area) originate from $\Gamma_{O_2} = 1 \times 10^{-10}$-$1 \times 10^{-9}$.

of the iron(III) fraction with a local minimum of β occurring at $t = 44\,\text{min}$. This is also apparent in the measurement data. A steady state β for $t \geq 50\,\text{min}$ was also predicted in agreement with our observations. Here, the uncertainty (blue region) stemmed from Γ_{O_2} values ranging between 1×10^{-10} and 1×10^{-9}, with the optimal fit at $\Gamma_{O_2} = 3.5 \times 10^{-10}$. In particular, the uncertainty range in the model from $\beta = 0.4 - 1$ is much larger than our experimental error bars and points to the high sensitivity of multiphase photochemical redox reactions to O_2 in the condense phase as well as Cu and Fe coupled reactions such as free iron and in an organic complex.

To provide an explanation for these findings, we also calculated the concentrations of O_2, CCFR (($^\bullet C_5H_5O_5)^{2-}$) and ROS in Figures 17 and G2 in the SI. The ROS levels (Figure 17a) stabilize at a steady state concentration at $t > 40\,\text{min}$, with H_2O_2, decreasing to a minimum, and OH, HO_2 and O_2^- increasing overall. The CCFR concentration did not deplete immediately after the UV light was turned off, but instead decayed from $7 \times 10^{-3}\,\text{mol L}-1$ at $t = 10\,\text{min}$ to zero at $\approx 40\,\text{min}$. The behavior mirrored the concentration of O_2, indicating that O_2 was consumed by the CCFR. Reaction R39 produces Cu^+, which reduced O_2 to O_2^- via R29, preventing the O_2 concentration from rising resulting in a slow decay of CCFR and maintaining a high value. This behavior also coincided with high H_2O_2 levels at $t \leq 45\,\text{min}$ due to Cu^+-ROS reactions R31 and R32.

The oxidation of Fe^{2+} by Cu^{2+} (R39) was essential to model the reoxidation of Fe^{III}(Cit):Cu^{II}(HCit):CA particles under high humidity conditions. These reactions enhanced overall turnover under light, making the supply of O_2 an important factor. CCFRs were a transient intermediate that strongly constrained O_2 reaction and diffusion to the entirety of the particle. We acknowledge that simply allowing Γ_{O_2} to vary is not a rigorous approach to account for reaction or diffusion limitations, which may also affect other reactions. These limitations contribute to the uncertainty in Γ_{O_2} and to the slight differences between
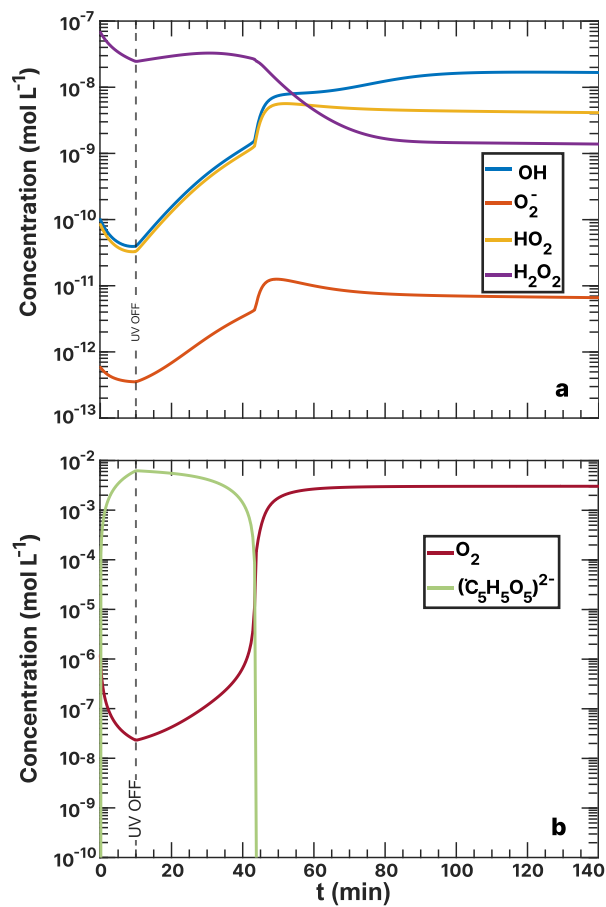
Figure 17. Modeled concentration of $Fe^{III}(Cit):Cu^{II}(HCit):CA = 1:0.02:1$ simulation including R38 and R39 from Table 6. **a** ROS concentrations. **b** Oxygen (O_2) and CCFR (($^\bullet C_5H_5O_5)^{-2}$) concentrations.

model runs. Future work could apply a multilayer model to resolve them and explore reaction and diffusion limitations further.

4 Conclusions

Using scanning transmission X-ray microscopy (STMX/NEXAFS), we observed novel redox characteristics in photochemically aged iron-copper complexed citric acid (CA) particles. A kinetic model was employed to explore the chemical mechanisms that led to the altered iron reoxidation pattern compared to systems without copper. The STXM/NEXAFS data provided evidence that the reoxidation of UV-light reduced iron(II) to iron(III) cause iron(III) fractions, β, to be elevated both on the surface and within the center of the particles, unlike pure iron-doped CA particles (Fe^{III}(Cit)/CA) (Alpert et al., 2021). Furthermore, at moderate relative humidity (RH = 60%), β in Fe^{III}(Cit)/Cu^{II}(HCit)/CA particles remained high immediately following UV irradiation.

Using a kinetic box model, we found that the changes in the photochemical aging process of Fe^{III}(Cit)/Cu^{II}(HCit)/CA particles observed in anoxic STXM/NEXAFS experiments at RH = 60% originated from a lower iron(II) quantum yield (ϕ) of the initial Fe^{III}(Cit) photolysis and a faster iron reoxidation, compared to Fe^{III}(Cit)/CA particles. By employing the newly fitted parameter, $\phi = 0.1$, we subsequently modeled UV aging experiments in the presence of oxygen. The model simulations of low humidity experiments (RH = 20 and 47%), running on Cu-ROS and Cu-Fe coupling reactions taken from the literature, successfully replicated the experimental data. However, experiments carried out at RH = 60% using different mole ratios of copper (M_r of Fe^{III}(Cit) : Cu^{II}(HCit) : CA = 1:0.2:1 and 1:0.02:1) could not be replicated using the same chemical mechanism. The modeled value of β immediately after UV irradiation was underestimated by ≈ 0.4, reaching only $\beta = 0.9$ after 90 min of reoxidation. The predicted oxygen concentration suggested that limitations in its uptake coefficient (Γ_{O_2}) could not account for the fast iron(III) reoxidation. Thus, at elevated humidity, an as yet undescribed chemical process likely accelerated the reoxidation of copper-containing particles.

Reactions between copper(II) and iron(II), reoxidizing iron(II) even during UV light exposure, proved crucial to improving the model's performance. Previous studies have demonstrated copper-iron interactions in both solid phase (Ammann et al., 1992; Goh et al., 2006) and aqueous phase chemistry (Matocha et al., 2005). In this work, we hypothesize that such coupling may also occur in mixed Cu-Fe polynuclear citrate complexes. To test this, we included two direct reactions oxidizing iron(II) to iron(III) while reducing copper(II) to copper(I) and adjusted their rate constants accordingly. Incorporating these reactions greatly improved the simulations, and the new model runs displayed an oscillating β pattern that began during UV aging, closely mirroring the STXM/NEXAFS observations for more than an hour of dark reoxidation.

This work emphasizes again the important role of condensed phase radical production via chromophores absorbing in the UVA range. While Mao et al. (2013) indicated that gas phase HO$_2$ and H$_2$O$_2$ influxes into the condensed phase may be significantly higher than their internal production rates, we arrive at a different conclusion here, as already pointed out by Arroyo et al. (2018) for HO$_2$ production initiated by aromatic carbonyl photosensitizers. Uptake of gas phase HO$_2$ to aqueous particles is driven by the self-reaction of HO$_2$ and by the reaction with transition metal ions (TMI). Following the recommendation by IUPAC (Ammann et al., 2013) with its most recent updates available at iupac.aeris-data.fr, γ is around 1×10^{-2} for moderately acidic aerosol, TMI content in the mM range (Al-Abadleh, 2024) and particle diameters of $d = 500\,\text{nm}$. With an HO$_2$ concentration in the gas phase of $1 \times 10^8\,\text{cm}^{-3}$ an influx of HO$_2$ of $1.8 \times 10^{-6}\,\text{M}^{-1}\text{s}^{-1}$ is obtained. This influx

is almost three orders of magnitude lower compared to our modelled HO_2 production rate in the condensed phase of about $5 \times 10^{-4} \, M^{-1}s^{-1}$. And even when comparing to an extreme case with TMI content of $1 \, M$ and thus an order of magnitude larger HO_2 uptake, the internal HO_2 production remains higher. Thus even in presence of copper, the internal HO_2 production remains very important.

This study highlights the importance of understanding detailed chemical mechanisms for accurately depicting aerosol photochemical aging. Individual chemical species, such as copper, can significantly influence these processes in surprising ways, especially in organic aerosols that interact with trace compounds throughout their atmospheric lifetime. Anthropogenic emissions add further complexity to these photochemical aging mechanisms. Further work should focus on multiphase modeling approaches that link chemistry with physical characteristics and extend these mechanisms to ambient secondary organic aerosol particles.

Code and data availability. The data and codes that support the findings of this study are publicly available at https://doi.org/10.5281/zenodo.14065174.

A1 STXM/NEXAFS iron spectra
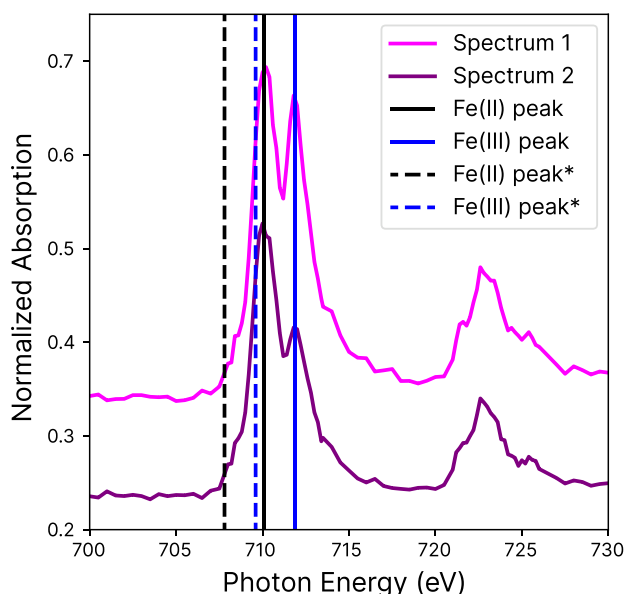
Figure A1. Iron arbsorption as a function of photon energies over the the L-edge with the iron(II) (black) and iron(III) (blue) absorption peaks (straight lines). The peaks were calibrated with measurements by Moffet et al. (2012) (stared) and they differed by $2.3 \, eV$. Two independently measured spectra are shown.

B1   Sun actinic flux vs STXM LED

Table B1. Results of the actinic flux/LED flux factor (ζ) with Eq. 2 for all possible combinations shown in Fig. B1.

Sun condition	Power	Wavelength	factor, ζ
Summer LA	1 V	270-500 nm	106.5
Winter LA	1 V	270-500 nm	57.3
Summer LA	7 V	270-500 nm	18.6
Winter LA	7 V	270-500 nm	10.0
Summer LA	1 V	350-400 nm	19.9
Winter LA	1 V	350-400 nm	10.4
Summer LA	7 V	350-400 nm	3.5
Winter LA	7 V	350-400 nm	1.8
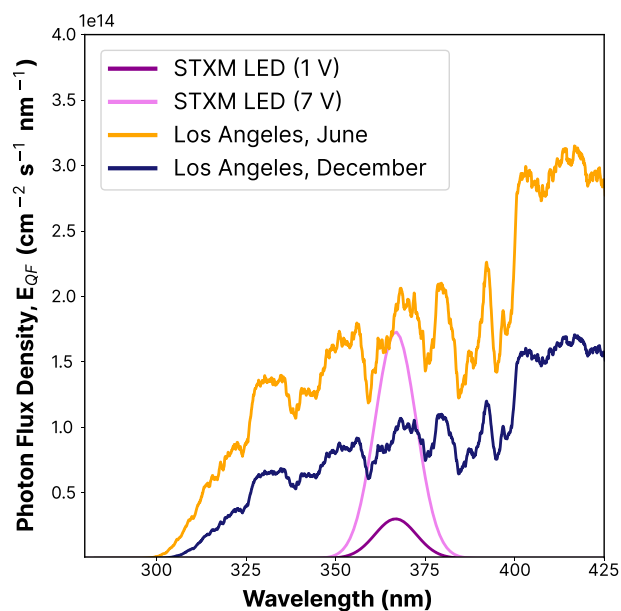
Figure B1. UV LED spectra flux density used for UV-aging in STXM/NEXAFS experiments for the 1 V (magenta) and 7 V setting (violet), and solar spectral flux densities in Los Angeles in June (orange) and December (dark blue) measured at noon as a function of the integrated UV-wavelength range (λ = 270-500 nm, see Eq. 2). The flux densities of the actinic spectra are taken from the *libRadtran* software Emde et al. (2016).

C1 Iron(III) reduction with light
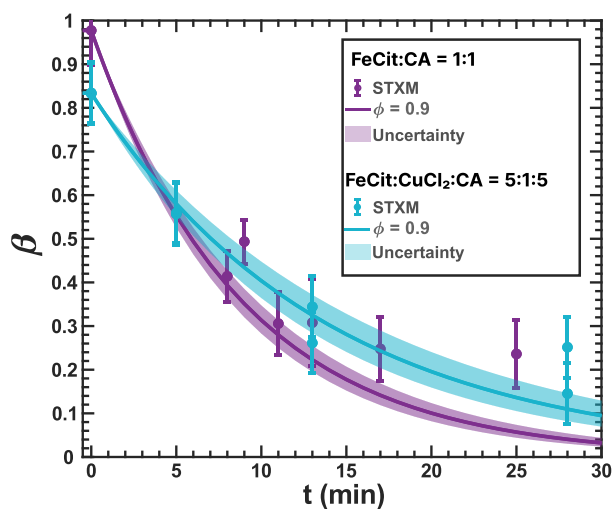
Figure C1. Iron(III) fraction, β, as a function of time irradiated with UV light from the LED with a narrow wavelength band centered at $370\,\mathrm{nm}$. The plot shows circles and lines as measurements and model output, respectively. Violet data and model output are from a previous study using $Fe^{III}(Cit)/CA$, and modeled using a photolysis frequency, $j = (2.2 \pm 0.2) \times 10^{-3}\,\mathrm{s^{-1}}$ (Dou et al., 2021). The light blue measurements, performed in the environmental cell without O_2 and RH = 0%, and model output are from this work, using $Fe^{III}(Cit):CuCl_2:$ CA at a $1:0.2:1$ mole ratio, with $j = (1.26 \pm 0.20) \times 10^{-3}\,\mathrm{s^{-1}}$. An iron(II) quantum yield, $\phi = 0.9$, was used to calculate j. Error bars are ± 0.07 or propagated from the photon counting error, whichever is larger.

D1 Additional iron reoxidation experiments
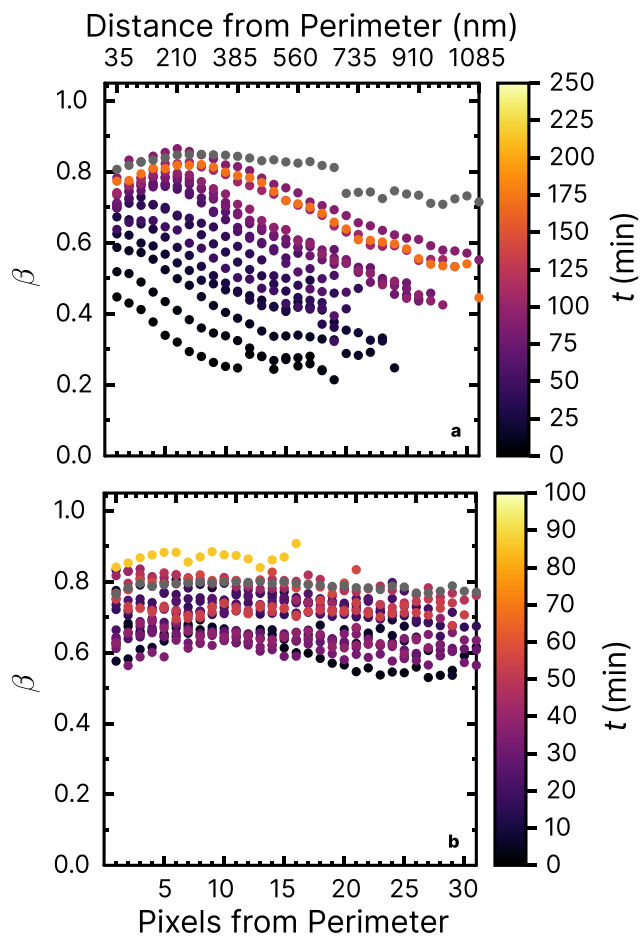
Figure D1. Iron(III) fraction, β, with increasing reoxidation time, t, after the irradiation for $10\,\mathrm{min}$ at a photolysis frequency of $j = (8.1 \pm 0.2) \times 10^{-3}\,\mathrm{s}^{-1}$ and with a mole ratio of $\mathrm{Fe^{III}(Cit):Cu^{II}(HCit):CA} = 1:0.02:1$. RH $= 47\%$ (a) and 60% (b). Please note the different color bars for the reoxidation time, t.
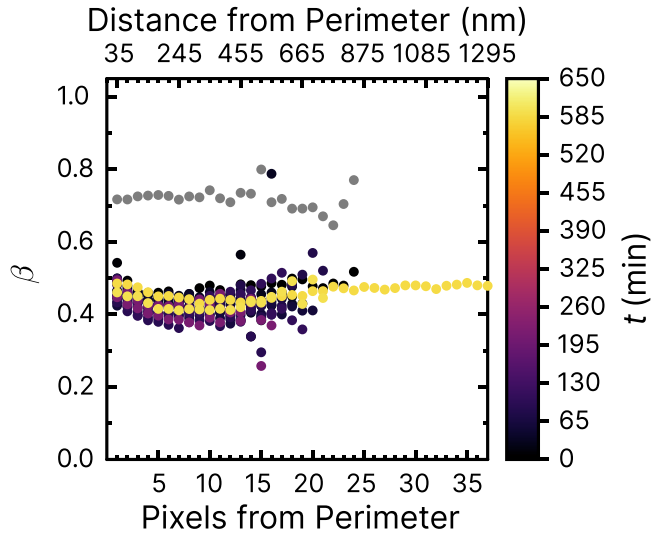
Figure D2. Iron(III) fraction, β, with increasing reoxidation time, t, after the irradiation for $10\,\mathrm{min}$ at a photolysis frequency of $j = (8.1 \pm 0.2) \times 10^{-3}\,\mathrm{s}^{-1}$ and RH = 20% with a mole ratio of $\mathrm{Fe}^{\mathrm{III}}(\mathrm{Cit}) : \mathrm{Cu}^{\mathrm{II}}(\mathrm{HCit}) : \mathrm{CA} = 1 : 0.2 : 1$.

E1 Particle Concentration

E1.1 Density of solution

The density of the solution is dependent on the mass fraction of iron citrate and CA in the film. we start with the density of CA as a function of its mass fraction ($\rho_{ca(mfs)}$). This is measured by Lienhard et al. (2012) and fitted according to Eq. E1.

$$\rho_{ca(mfs)} = 0.9971 + d_1 \cdot mfs + d_2 \cdot mfs^2 \tag{E1}$$

the mfs corresponds to a certain RH in terms of water activity (a_w) and is parameterized as follows:

$$a_w(mfs) = \frac{1 - mfs}{1 + q \cdot mfs + r \cdot mfs^2} \tag{E2}$$

An interpolation of eq. E2 gives us the exact mass fraction of CA, which we insert in Eq. E1. iron citrate is not parameterized in the literature. However, Dou et al. (2021) has determined the water activity of an aqueous $1m\ \mathrm{Fe}^{\mathrm{III}}(\mathrm{cit})$ solution and found that this water activity corresponds to that of an $0\,81m$ aqueous CA solution. To correct for this, we need to assume that everything is considered CA. We use a variable, n_{cit}, which represents the apparent moles of citrate with the correction factor introduced above:

$$n_{\mathrm{cit}} = n_{\mathrm{ca}} + 0.81 \cdot n_{\mathrm{fecit}} + 0.81 \cdot n_{\mathrm{cucit}} \tag{E3}$$

the mass of the total solution assuming that everything is citric acid results in:

$$m_{\mathrm{cit}} = n_{\mathrm{cit}} \cdot m_{\mathrm{ca}} \tag{E4}$$

This follows in the mass of water:

$$m_{h_2o} = m_{cit} \cdot \frac{(1 - mfs_{ca})}{mfs_{ca}}, \tag{E5}$$

leading to the total mass of the solution in the flowtube (mass of the equilibrated film):

$$m_{film} = m_{ca} + m_{fecit} + m_{cucit} + m_{h_2o} \tag{E6}$$

It should be noted that these masses need to be proportionally scaled to those used to coat the flowtube. The actual mass fraction of the solute is then given by:

$$mfs_{sol} = \frac{m_{ca} + m_{fecit} + m_{cucit}}{m_{ca} + m_{fecit} + m_{cucit} + m_{h_2o}} \tag{E7}$$

The density of the equilibrated solution is calculated as a weighted mean of the dry densities times the density of CA as a function of the mass fraction of solute (mfs):

$$\rho_{sol(mfs)} = \rho_{ca(mfs)} \cdot \left(\frac{n_{ca} + n_{fecit} \cdot r_{fecit} + n_{cucit} \cdot r_{cucit}}{n_{ca} + n_{fecit} + n_{cucit}} \right), \tag{E8}$$

whereas r_{fecit} (r_{cucit}) denote the ratios between the dry iron (copper) density and the dry density of CA.

E1.2 Concentrations

The number density (c) of CA, FeCit, CuCit and H_2O can now be calculated with the density of the solution and its mole ratio (a_1, a_2, ... in Eq. E12):

$$c_{ca} = n_a \cdot \left(\frac{\rho_{sol} \cdot mfs_{sol}}{m_{ca} + a_3 \cdot m_{fecit} + a_4 \cdot m_{cucit}} \right) \tag{E9}$$

$$c_{fecit} = n_a \cdot \left(\frac{\rho_{sol} \cdot mfs_{sol}}{a_1 \cdot m_{ca} + m_{fecit} + a_2 \cdot m_{cucit}} \right) \tag{E10}$$

$$c_{cucit} = n_a \cdot \left(\frac{\rho_{sol} \cdot mfs_{sol}}{a_5 \cdot m_{ca} + a_6 \cdot m_{fecit} + m_{cucit}} \right) \tag{E11}$$

$$c_{h_2o} = n_a \cdot \left(\frac{\rho_{sol} \cdot (1 - mfs_{sol})}{m_{h_2o}} \right), \tag{E12}$$

where:

$$a_1 = \frac{n_{ca}}{n_{fecit}}$$

$$a_2 = \frac{n_{cucit}}{n_{fecit}}$$

$$a_3 = \frac{n_{fecit}}{n_{ca}}$$

$$a_4 = \frac{n_{cucit}}{n_{ca}}$$

$$a_5 = \frac{n_{ca}}{n_{cucit}}$$

$$a_6 = \frac{n_{fecit}}{n_{cucit}}$$

F1 Fe^{III}(Cit)/CA reaction turnovers and concentration profiles
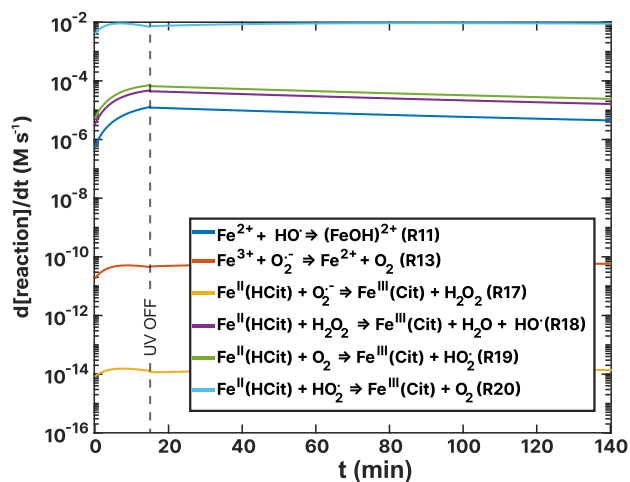
Figure F1. Turnover rates (d[reaction]/dt) as a function of time, t, of Fe^{II}(HCit) and Fe^{II}/Fe^{III} ion loss reactions of the Fe^{III}(Cit):CA = 1:10 simulation of the (RH = 60%) experiment as listed in Table 3. UV radiation is turned off at t = 15 min.
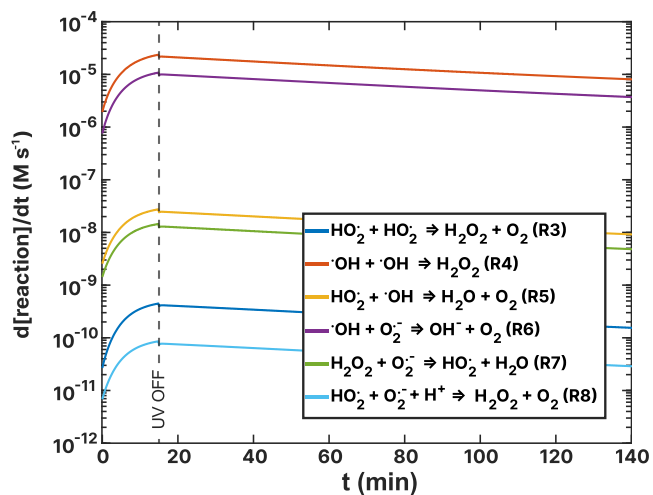
Figure F2. Turnover rates (d/dt) of the ROS reactions listed in Table 3 as a function of time, t, of the Fe^{III}(Cit):CA = 1:10 experiment (a) and the Fe^{III}(Cit):Cu^{II}(HCit):CA = 1:0.2:1 experiment (b) simulations. UV radiation was turned off at t = 15 min.
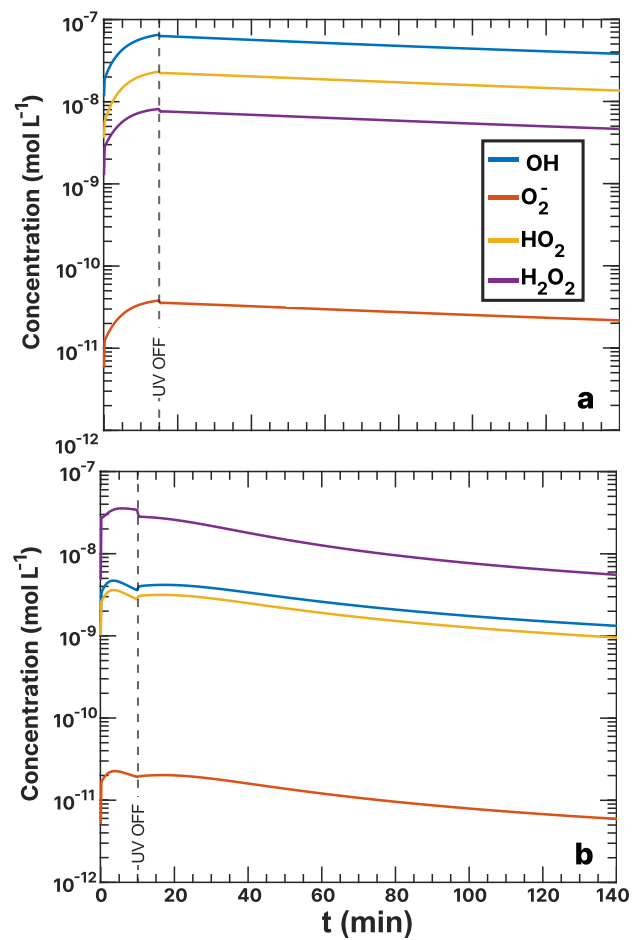
Figure F3. ROS concentrations during $Fe^{III}(Cit):CA = 1:10$ (**a**) and $Fe^{III}(Cit):Cu^{II}(HCit):CA = 1:0.2:1$ (**b**) experiment simulation as a function of time. UV radiation was turned off at $t = 15\,min$ (**a**) and $10\,min$ (**b**).
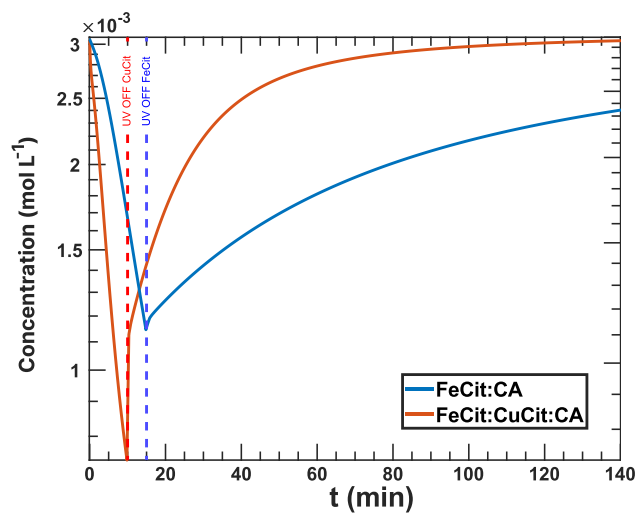
Figure F4. Oxygen concentrations during the $Fe^{III}(Cit):CA = 1:10$ and the $Fe^{III}(Cit):Cu^{II}(HCit):CA = 1:0.2:1$ experiment under RH = 60% simulation as a function of time. UV radiation was turned off at $t = 10\,min$ and $15\,min$, respectively.

G1 Simulations of Cu^{2+} reduced reoxidation reactions of $Fe^{III}(Cit):Cu^{II}(HCit):CA = 1:0.2:1$ samples
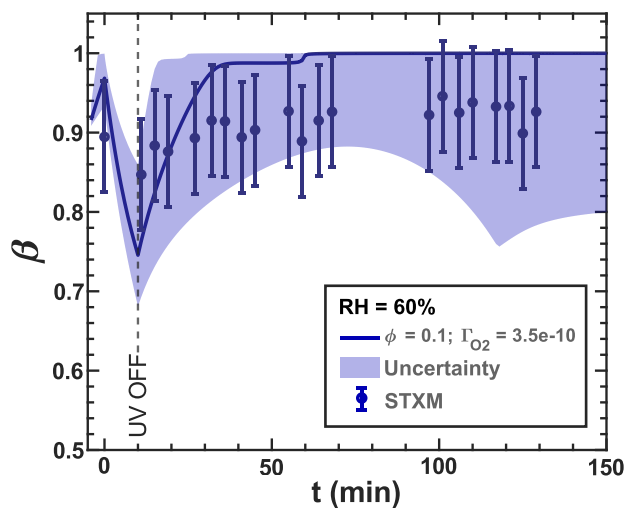
Figure G1. Iron(III) fraction, β, with increasing dark reoxidation time (t) after UV radiation ($t = 10$ min). $Fe^{III}(Cit):Cu^{II}(HCit):CA = 1:0.2:1$ samples. The circles with error bars represent the average of all particles mapped at one time step during the STXM experiments, and the straight lines express the Kintecus model output. The O_2 uptake coefficients (Γ_{O_2}) were determined from the initial $Fe^{III}(Cit)/CA$ mechanism (see Section 2.5). The lower and upper boundary of the model uncertainty (blue area) originate from $\Gamma_{O_2} = 1 \times 10^{-10}$-$1 \times 10^{-9}$. The iron(II) quantum yield (ϕ) was adapted from the anoxic experiment shown in Figure 11, optimized towards the new Cu^{2+} induced reoxidation reaction rates, and multiplied by the photolysis frequency ($j = (8.1 \pm 1.0) \times 10^{-3}\,\text{s}^{-1}$). The reaction rates for R38 was $2 \times 10^6\,\text{M}^{-1}\text{s}^{-1}$ and for R39 $7 \times 10^8\,\text{M}^{-1}\text{s}^{-1}$. Uncertainty in the experimental derived β was determined as, $\Delta\beta = \pm 0.07$.
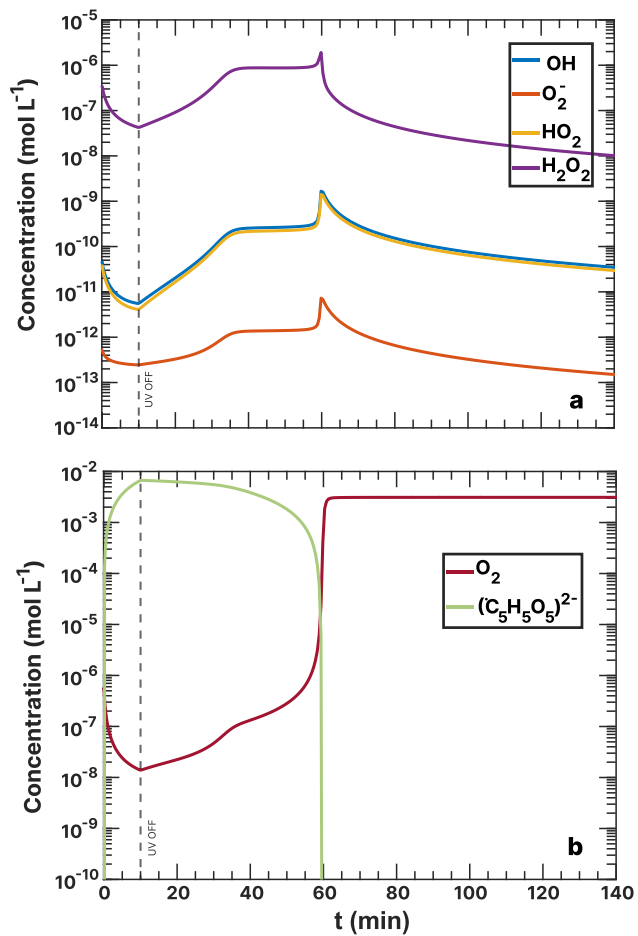
Figure G2. Concentration results of $Fe^{III}(Cit):Cu^{II}(HCit):CA = 1:0.2:1$ simulation including R38 and R39 from Table 6. **a** ROS concentrations. **b** Oxygen (O_2) and CCFR (($^\bullet C_5H_5O_5)^{-2}$) concentrations.

G2 Calculation of diffuso-reactive length for O_2

We know from Hanson et al. (1994) that the reacto-diffusive length is defined as:

$$l_D = \sqrt{\frac{D_l}{k^I}}, \tag{G1}$$

whereas D_l is the liquid phase diffusion coefficient (taken from Dou et al. (2021)) and k^I describes the sum of the oxygen sinks corresponding to the turnover rate of reaction R2 in Table 3 ($3.9 \times 10^{-2}\,\mathrm{M\,s^{-1}}$) as the other sink reaction with iron(II)Cit (R19) has a first order reaction rate six orders of magnitudes lower than R2 divided by the O_2 concentration in steady state (C_{ss} in $moles$, taken from Figure F4). In this case, it is equivalent to:

$$k^I = \frac{k^{R2}}{C_{ss}}, \tag{G2}$$

This leads to a diffuso-reactive length, l_D, for oxygen of $5.26 \times 10^{-9}\,$m ($5.3\,$nm). If we assume an aqueous phase dimension of the particle radii, which are about $100\text{-}500\,$nm, we can argue that this is much bigger than the diffuso-reactive length of oxygen and thus claim that the reoxidation system is underlying a diffusion-limited regime.
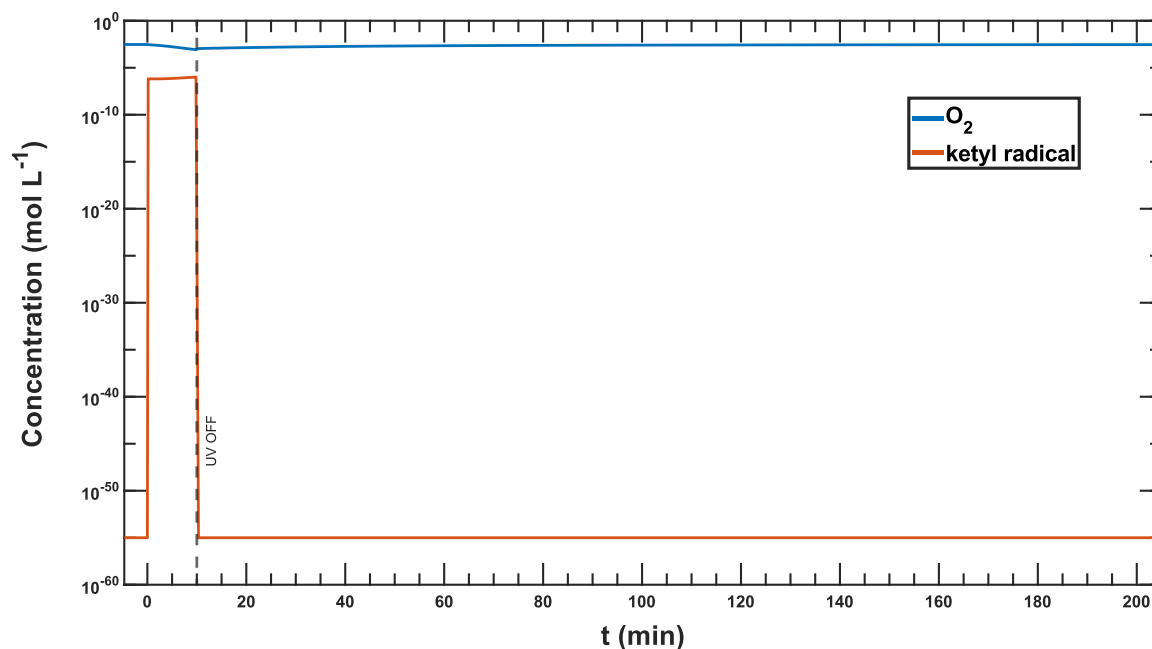
Figure G3. Oxygen and ketyl radical ($(^{\bullet}C_5H_5O_5)^{-2}$) concentration in a $Fe^{III}(Cit):Cu^{II}(HCit):CA = 1:0.2:1$ simulation at RH = 65% used for the calculation of the diffuso-reactive length with Equations G1 and G2.

Author contributions. MA, PAP and KK designed the research. LT, RKYC, PAP and KK carried out the STXM/NEXAFS measurements. PAP and KK did the modeling work with valuable inputs by MA. KK wrote the manuscript with significant inputs by PAP and MA.

Competing interests. At least one of the (co-)authors is a member of the editorial board of Atmospheric Chemistry and Physics

Acknowledgements. The authors thank the Swiss National Science Foundation for financial support with grants no. 188662 and 189883.
565 The authors thank Prof. Christian Ludwig for having facilitated this work and LT's salary was funded by the Swiss National Foundation (project no. 184817). In situ electron and X-ray absorption spectroscopy experiments were hosted at the POLLUX Beamline at the Swiss Light Source (SLS), the support of which is highly appreciated.

References

Abida, O., Kolar, M., Jirkovsky, J., and Mailhot, G.: Degradation of 4-chlorophenol in aqueous solution photoinduced by Fe(iii)-citrate complex, Photochemical and Photobiological Sciences, 11, 794–802, https://doi.org/10.1039/c2pp05358f, 2012.

Abrahamson, H. B., Rezvani, A. B., and Brushmiller, J. G.: Photochemical and spectroscopic studies of complexes, of iron(III) with citric acid and other carboxylic acids, Inorganica Chimica Acta, 226, 117–127, https://doi.org/10.1016/0020-1693(94)04077-X, 1994.

Al-Abadleh, H. A.: Review of the bulk and surface chemistry of iron in atmospherically relevant systems containing humic-like substances, RSC Advances, 5, 45 785–45 811, https://doi.org/10.1039/c5ra03132j, 2015.

Al-Abadleh, H. A.: Iron content in aerosol particles and its impact on atmospheric chemistry, Chemical Communications, 60, 1840–1855, https://doi.org/10.1039/d3cc04614a, 2024.

Alpert, P. A., Arroyo, P. C., Dou, J., Krieger, U. K., Steimer, S. S., Förster, J. D., Ditas, F., Pöhlker, C., Rossignol, S., Passananti, M., Perrier, S., George, C., Shiraiwa, M., Berkemeier, T., Watts, B., and Ammann, M.: Visualizing reaction and diffusion in xanthan gum aerosol particles exposed to ozone, Physical Chemistry Chemical Physics, 21, 20 613–20 627, https://doi.org/10.1039/c9cp03731d, 2019.

Alpert, P. A., Dou, J., Arroyo, P. C., Schneider, F., Xto, J., Luo, B., Peter, T., Huthwelker, T., Borca, C. N., Henzler, K. D., Schaefer, T., Herrmann, H., Raabe, J., Watts, B., Krieger, U. K., and Ammann, M.: Photolytic radical persistence due to anoxia in viscous aerosol particles, Nature Communications 2021 12:1, 12, 1–8, https://doi.org/10.1038/s41467-021-21913-x, 2021.

Ammann, M., Hauert, R., and Burtscher, H.: In situ detection of monovalent copper in aerosols by photoemission, Fresenius' Journal of Analytical Chemistry, 343, 491–496, https://doi.org/10.1007/BF00322156, 1992.

Ammann, M., Cox, R. A., Crowley, J. N., Jenkin, M. E., Mellouki, A., Rossi, M. J., Troe, J., and Wallington, T. J.: Evaluated kinetic and photochemical data for atmospheric chemistry: Volume VI - Heterogeneous reactions with liquid substrates, Atmospheric Chemistry and Physics, https://doi.org/10.5194/acp-13-8045-2013, 2013.

Arroyo, P. C., Malecha, K. T., Ammann, M., and Nizkorodov, S. A.: Influence of humidity and iron(iii) on photodegradation of atmospheric secondary organic aerosol particles, Physical Chemistry Chemical Physics, https://doi.org/10.1039/c8cp03981j, 2018.

Bates, J. T., Fang, T., Verma, V., Zeng, L., Weber, R. J., Tolbert, P. E., Abrams, J. Y., Sarnat, S. E., Klein, M., Mulholland, J. A., and Russell, A. G.: Review of Acellular Assays of Ambient Particulate Matter Oxidative Potential: Methods and Relationships with Composition, Sources, and Health Effects, Environmental Science and Technology, 53, 4003–4019, https://doi.org/10.1021/acs.est.8b03430, 2019.

Benkelberg, H. J. and Warneck, P.: Photodecomposition of iron(III) hydroxo and sulfato complexes in aqueous solution: Wavelength dependence of OH and quantum yields, Journal of Physical Chemistry, 99, 5214–5221, https://doi.org/10.1021/j100014a049, 1995.

Berdnikov, V.: Catalytic activity of the hydrated copper ion in the decomposition of hydrogen peroxide, Russian Journal of Physical Chemistry, 47, 1060–1162, 1973.

Berkemeier, T., Huisman, A. J., Ammann, M., Shiraiwa, M., Koop, T., and Pöschl, U.: Kinetic regimes and limiting cases of gas uptake and heterogeneous reactions in atmospheric aerosols and clouds: A general classification scheme, Atmospheric Chemistry and Physics, https://doi.org/10.5194/acp-13-6663-2013, 2013.

Bielski, B. H. J., Cabelli, D. E., Arudi, R. L., and Ross, A. B.: Reactivity of HO2/O2 Radicals in Aqueous Solution, Journal of Physical and Chemical Reference Data, 14, 1041–1100, https://doi.org/10.1063/1.555739, 1985.

Bjergbakke, E., Sehested, K., and Rasmussen, O. L.: The Reaction Mechanism and Rate Constants in the Radiolysis of Fe 2+ -Cu 2+ Solutions, Radiation Research, https://doi.org/10.2307/3574449, 1976.

Brandt, C. and van Eldik, R.: Transition Metal-Catalyzed Oxidation of Sulfur(IV) Oxides. Atmospheric-Relevant Processes and Mechanisms, Chemical Reviews, 95, 119–190, https://doi.org/10.1021/cr00033a006, 1995.

Charrier, J. G. and Anastasio, C.: Rates of Hydroxyl Radical Production from Transition Metals and Quinones in a Surrogate Lung Fluid, Environmental Science and Technology, 49, 9317–9325, https://doi.org/10.1021/acs.est.5b01606, 2015.

Charrier, J. G., McFall, A. S., Richards-Henderson, N. K., and Anastasio, C.: Hydrogen peroxide formation in a surrogate lung fluid by transition metals and quinones present in particulate matter, Environmental Science and Technology, https://doi.org/10.1021/es501011w, 2014.

Chifflet, S., Guyomarc'h, L., Dominutti, P., Heimbürger-Boavida, L. E., Angeletti, B., Louvat, P., Jaffrezo, J. L., Vu, C. T., Uzu, G., and Mari, X.: Seasonal variations of metals and metalloids in atmospheric particulate matter (PM2.5) in the urban megacity Hanoi, Atmospheric Pollution Research, 15, https://doi.org/10.1016/j.apr.2023.101961, 2024.

Christensen, H. and Sehested, K.: Pulse radiolysis at high temperatures and high pressures, Radiation Physics and Chemistry, https://doi.org/10.1016/0146-5724(81)90195-3, 1981.

Christensen, H., Sehested, K., and Corfitzen, H.: Reactions of hydroxyl radicals with hydrogen peroxide at ambient and elevated temperatures, Journal of Physical Chemistry, 86, 1588–1590, https://doi.org/10.1021/j100206a023, 1982.

Cieśla, P., Kocot, P., Mytych, P., and Stasicka, Z.: Homogeneous photocatalysis by transition metal complexes in the environment, Journal of Molecular Catalysis A: Chemical, 224, 17–33, https://doi.org/10.1016/j.molcata.2004.08.043, 2004.

Corral Arroyo, P., Bartels-Rausch, T., Alpert, P. A., Dumas, S., Perrier, S., George, C., and Ammann, M.: Particle-Phase Photosensitized Radical Production and Aerosol Aging, Environmental Science and Technology, https://doi.org/10.1021/acs.est.8b00329, 2018.

Corral Arroyo, P., David, G., Alpert, P. A., Parmentier, E. A., Ammann, M., and Signorell, R.: Amplification of light within aerosol particles accelerates in-particle photochemistry, Science, 376, 293–296, https://doi.org/10.1126/science.abm7915, 2022.

Daellenbach, K. R., Uzu, G., Jiang, J., Cassagnes, L. E., Leni, Z., Vlachou, A., Stefenelli, G., Canonaco, F., Weber, S., Segers, A., Kuenen, J. J., Schaap, M., Favez, O., Albinet, A., Aksoyoglu, S., Dommen, J., Baltensperger, U., Geiser, M., El Haddad, I., Jaffrezo, J. L., and Prévôt, A. S.: Sources of particulate-matter air pollution and its oxidative potential in Europe, Nature, https://doi.org/10.1038/s41586-020-2902-8, 2020.

De Laat, J. and Le, T. G.: Kinetics and modeling of the Fe(III)/H2O2 system in the presence of sulfate in acidic aqueous solutions, Environmental Science and Technology, 39, 1811–1818, https://doi.org/10.1021/es0493648, 2005.

Deguillaume, L., Leriche, M., Desboeufs, K., Mailhot, G., George, C., and Chaumerliac, N.: Transition metals in atmospheric liquid phases: Sources, reactivity, and sensitive parameters, Chemical Reviews, https://doi.org/10.1021/cr040649c, 2005.

Dellinger, B., Pryor, W. A., Cueto, R., Squadrito, G. L., Hegde, V., and Deutsch, W. A.: Role of free radicals in the toxicity of airborne fine particulate matter, Chemical Research in Toxicology, 14, 1371–1377, https://doi.org/10.1021/tx010050x, 2001.

D'Huysser, A., Lerebours-Hannoyer, B., Lenglet, M., and Bonnelle, J. P.: La spectroscopie de photoélectrons induits par rayons X et la répartition des ions cuivre Cu+ et Cu2+ dans les ferrites de cuivre, Journal of Solid State Chemistry, 39, 246–256, https://doi.org/10.1016/0022-4596(81)90338-8, 1981.

Dou, J., Alpert, P. A., Corral Arroyo, P., Luo, B., Schneider, F., Xto, J., Huthwelker, T., Borca, C. N., Henzler, K. D., Raabe, J., Watts, B., Herrmann, H., Peter, T., Ammann, M., and Krieger, U. K.: Photochemical degradation of iron(III) citrate/citric acid aerosol quantified with the combination of three complementary experimental techniques and a kinetic process model, Atmospheric Chemistry and Physics, 21, 315–338, https://doi.org/10.5194/ACP-21-315-2021, 2021.

Emde, C., Buras-Schnell, R., Kylling, A., Mayer, B., Gasteiger, J., Hamann, U., Kylling, J., Richter, B., Pause, C., Dowling, T., and Bugliaro, L.: The libRadtran software package for radiative transfer calculations (version 2.0.1), Geoscientific Model Development, 9, 1647–1672, https://doi.org/10.5194/gmd-9-1647-2016, 2016.

Ervens, B., George, C., Williams, J. E., Buxton, G. V., Salmon, G. A., Bydder, M., Wilkinson, F., Dentener, F., Mirabel, P., Wolke, R., and Herrmann, H.: CAPRAM 2.4 (MODAC mechanism): An extended and condensed tropospheric aqueous phase mechanism and its application, Journal of Geophysical Research D: Atmospheres, https://doi.org/10.1029/2002jd002202, 2003.

Faust, C. and Zepp, R. G.: Photochemistry of Aqueous Iron(III) -Polycarboxylate Complexes: Roles in the Chemistry of Atmospheric and Surface Waters, Environmental Science and Technology, pp. 2517–2522, 1993.

Fenton, H. J.: Oxidation of tartaric acid in presence of iron, https://doi.org/10.1039/CT8946500899, 1894.

George, C., Ammann, M., D'Anna, B., Donaldson, D. J., and Nizkorodov, S. A.: Heterogeneous Photochemistry in the Atmosphere, https://doi.org/10.1021/cr500648z, 2015.

Glebov, E. M., Pozdnyakov, I. P., Grivin, V. P., Plyusnin, V. F., Zhang, X., Wu, F., and Deng, N.: Intermediates in photochemistry of Fe(iii) complexes with carboxylic acids in aqueous solutions, Photochemical and Photobiological Sciences, https://doi.org/10.1039/c0pp00151a, 2011.

Goh, S. W., Buckley, A. N., Lamb, R. N., Rosenberg, R. A., and Moran, D.: The oxidation states of copper and iron in mineral sulfides, and the oxides formed on initial exposure of chalcopyrite and bornite to air, Geochimica et Cosmochimica Acta, 70, 2210–2228, https://doi.org/10.1016/j.gca.2006.02.007, 2006.

Goldstein, S., Czapski, G., Cohen, H., and Meyerstein, D.: Deamination of β-alanine induced by hydroxyl radicals and monovalent copper ions. A pulse radiolysis study, Inorganica Chimica Acta, https://doi.org/10.1016/S0020-1693(00)83177-1, 1992.

Gonzalez, D. H., Cala, C. K., Peng, Q., and Paulson, S. E.: HULIS Enhancement of Hydroxyl Radical Formation from Fe(II): Kinetics of Fulvic Acid-Fe(II) Complexes in the Presence of Lung Antioxidants, Environmental Science and Technology, https://doi.org/10.1021/acs.est.7b01299, 2017.

Gracheva, M., Homonnay, Z., Singh, A., Fodor, F., Marosi, V. B., Solti, A., and Kovacs, K.: New aspects of the photodegradation of iron(III) citrate: spectroscopic studies and plant-related factors, Photochemical and Photobiological Sciences, 21, 983–996, https://doi.org/10.1007/s43630-022-00188-1, 2022.

Hallquist, M., Wenger, J. C., Baltensperger, U., Rudich, Y., Simpson, D., Claeys, M., Dommen, J., Donahue, N. M., George, C., Goldstein, A. H., Hamilton, J. F., Herrmann, H., Hoffmann, T., Iinuma, Y., Jang, M., Jenkin, M. E., Jimenez, J. L., Kiendler-Scharr, A., Maenhaut, W., McFiggans, G., Mentel, T. F., Monod, A., Prévôt, A. S., Seinfeld, J. H., Surratt, J. D., Szmigielski, R., and Wildt, J.: The formation, properties and impact of secondary organic aerosol: Current and emerging issues, Atmospheric Chemistry and Physics, https://doi.org/10.5194/acp-9-5155-2009, 2009.

Hanson, D. R., Ravishankara, A. R., and Solomon, S.: Heterogeneous reactions in sulfuric acid aerosols: a framework for model calculations, Journal of Geophysical Research, 99, 3615–3629, https://doi.org/10.1029/93JD02932, 1994.

Hemmes, P., Rich, L. D., Cole, D. L., and Eyring, E. M.: Kinetics of hydrolysis of ferric ion in dilute aqueous solution, Analytical Chemistry, 75, 929–932, https://doi.org/10.1021/ac60297a755, 1971.

Hong, S., Candelone, J. P., Soutif, M., and Boutron, C. F.: A reconstruction of changes in copper production and copper emissions to the atmosphere during the past 7000 years, Science of the Total Environment, 188, 183–193, https://doi.org/10.1016/0048-9697(96)05171-6, 1996.

Huang, R. J., Zhang, Y., Bozzetti, C., Ho, K. F., Cao, J. J., Han, Y., Daellenbach, K. R., Slowik, J. G., Platt, S. M., Canonaco, F., Zotter, P., Wolf, R., Pieber, S. M., Bruns, E. A., Crippa, M., Ciarelli, G., Piazzalunga, A., Schwikowski, M., Abbaszade, G., Schnelle-Kreis, J.,

680   Zimmermann, R., An, Z., Szidat, S., Baltensperger, U., El Haddad, I., and Prévôt, A. S.: High secondary aerosol contribution to particulate pollution during haze events in China, Nature, 514, 218–222, https://doi.org/10.1038/nature13774, 2015.

Hug, S. J., Canonica, L., Wegelin, M., Gechter, D., and Von Gunten, U.: Solar oxidation and removal of arsenic at circumneutral pH in iron containing waters, Environmental Science and Technology, https://doi.org/10.1021/es001551s, 2001.

Huthwelker, T., Zelenay, V., Birrer, M., Krepelova, A., Raabe, J., Tzvetkov, G., Vernooij, M. G., and Ammann, M.: An in situ cell to study

685   phase transitions in individual aerosol particles on a substrate using scanning transmission x-ray microspectroscopy, Review of Scientific Instruments, https://doi.org/10.1063/1.3494604, 2010.

Ianni, J. C.: Kintecus, http://www.kintecus.com/, 2017.

Ito, A. and Miyakawa, T.: Aerosol Iron from Metal Production as a Secondary Source of Bioaccessible Iron, Environmental Science and Technology, 57, 4091–4100, https://doi.org/10.1021/acs.est.2c06472, 2023.

690   Jayson, G. G., Parsons, B. J., and Swallow, A. J.: Oxidation of ferrous ions by hydroxyl radicals, Journal of the Chemical Society, Faraday Transactions 1: Physical Chemistry in Condensed Phases, 68, 2053–2058, https://doi.org/10.1039/F19726802053, 1973.

Kieber, R. J., Williams, K., Willey, J. D., Skrabal, S., and Avery, G. B.: Iron speciation in coastal rainwater: concentration and deposition to seawater, Marine Chemistry, 73, 83–95, https://doi.org/10.1016/S0304-4203(00)00097-9, 2001.

Koop, T., Bookhold, J., Shiraiwa, M., and Pöschl, U.: Glass transition and phase state of organic compounds: Dependency on molecular

695   properties and implications for secondary organic aerosols in the atmosphere, Physical Chemistry Chemical Physics, 13, 19 238–19 255, https://doi.org/10.1039/c1cp22617g, 2011.

Kroll, J. H. and Seinfeld, J. H.: Chemistry of secondary organic aerosol: Formation and evolution of low-volatility organics in the atmosphere, https://doi.org/10.1016/j.atmosenv.2008.01.003, 2008.

Lelieveld, S., Wilson, J., Dovrou, E., Mishra, A., Lakey, P. S., Shiraiwa, M., Pöschl, U., and Berkemeier, T.: Hydroxyl Radical Production

700   by Air Pollutants in Epithelial Lining Fluid Governed by Interconversion and Scavenging of Reactive Oxygen Species, Environmental Science and Technology, 55, 14 069–14 079, https://doi.org/10.1021/acs.est.1c03875, 2021.

Lelieveld, S., Lelieveld, J., Mishra, A., Daiber, A., Pozzer, A., Pöschl, U., and Berkemeier, T.: Endogenous Nitric Oxide Can Enhance Oxidative Stress Caused by Air Pollutants and Explain Higher Susceptibility of Individuals with Inflammatory Disorders, Environmental Science and Technology, https://doi.org/10.1021/acs.est.3c07010, 2024.

705   Lienhard, D. M., Bones, D. L., Zuend, A., Krieger, U. K., Reid, J. P., and Peter, T.: Measurements of thermodynamic and optical properties of selected aqueous organic and organic-inorganic mixtures of atmospheric relevance, Journal of Physical Chemistry A, https://doi.org/10.1021/jp3055872, 2012.

Malecha, K. T. and Nizkorodov, S. A.: Photodegradation of Secondary Organic Aerosol Particles as a Source of Small, Oxygenated Volatile Organic Compounds, Environmental Science and Technology, 50, 9990–9997, https://doi.org/10.1021/acs.est.6b02313, 2016.

710   Mao, J., Fan, S., Jacob, D. J., and Travis, K. R.: Radical loss in the atmosphere from Cu-Fe redox coupling in aerosols, Atmospheric Chemistry and Physics, https://doi.org/10.5194/acp-13-509-2013, 2013.

Martell, A. E. and Smith, R. M.: Critical stability constants, Springer US, Boston, vol. 5 edn., 1982.

Matocha, C. J., Karathanasis, A. D., Rakshit, S., and Wagner, K. M.: Reduction of Copper(II) by Iron(II), Journal of Environmental Quality, 34, 1539–1546, https://doi.org/10.2134/jeq2005.0002, 2005.

715   Moffet, R. C., Henn, T., Laskin, A., and Gilles, M. K.: Automated chemical analysis of internally mixed aerosol particles using X-ray spectromicroscopy at the carbon K-edge, Analytical Chemistry, 82, 7906–7914, https://doi.org/10.1021/ac1012909, 2010.

Moffet, R. C., Furutani, H., Rödel, T. C., Henn, T. R., Sprau, P. O., Laskin, A., Uematsu, M., and Gilles, M. K.: Iron speciation and mixing in single aerosol particles from the Asian continental outflow, Journal of Geophysical Research Atmospheres, https://doi.org/10.1029/2011JD016746, 2012.

720   Perrin, D. D.: Stability Constants of Metal-Ion Complexes, Part B: Organic Ligands, IUPAC Chemical Data Series, 22, 1979.

Pham, A. N. and Waite, T. D.: Modeling the kinetics of Fe(II) oxidation in the presence of citrate and salicylate in aqueous solutions at pH 6.0-8.0 and 25°C, Journal of Physical Chemistry A, 112, 5395–5405, https://doi.org/10.1021/jp801126p, 2008.

Pöschl, U. and Shiraiwa, M.: Multiphase Chemistry at the Atmosphere-Biosphere Interface Influencing Climate and Public Health in the Anthropocene, Chemical Reviews, 115, 4440–4475, https://doi.org/10.1021/cr500487s, 2015.

725   Potter, P. M., Guan, X., and Lomnicki, S. M.: Synergy of iron and copper oxides in the catalytic formation of PCDD/Fs from 2-monochlorophenol, Chemosphere, 203, 96–103, https://doi.org/10.1016/j.chemosphere.2018.03.118, 2018.

Pozdnyakov, I. P., Kolomeets, A. V., Plyusnin, V. F., Melnikov, A. A., Kompanets, V. O., Chekalin, S. V., Tkachenko, N., and Lemmetyinen, H.: Photophysics of Fe(III)-tartrate and Fe(III)-citrate complexes in aqueous solutions, Chemical Physics Letters, https://doi.org/10.1016/j.cplett.2012.01.051, 2012.

730   Pozdnyakov, I. P., Melnikov, A. A., Tkachenko, N., Chekalin, S. V., Lemmetyinen, H., and Plyusnin, V. F.: Ultrafast photophysical processes for Fe(iii)-carboxylates, Dalton Transactions, 43, 17 590–17 595, https://doi.org/10.1039/c4dt01419g, 2014.

Raabe, J., Tzvetkov, G., Flechsig, U., Böge, M., Jaggi, A., Sarafimov, B., Vernooij, M. G., Huthwelker, T., Ade, H., Kilcoyne, D., Tyliszczak, T., Fink, R. H., and Quitmann, C.: PolLux: A new facility for soft x-ray spectromicroscopy at the swiss light source, Review of Scientific Instruments, https://doi.org/10.1063/1.3021472, 2008.

735   Rabani, J., Klug-Roth, D., and Lilie, J.: Pulse radiolytic investigations of the catalyzed disproportionation of peroxy radicals. Aqueous cupric ions, The Journal of Physical Chemistry, 77, 1169–1175, https://doi.org/10.1021/j100628a018, 1973.

Reid, J. P., Bertram, A. K., Topping, D. O., Laskin, A., Martin, S. T., Petters, M. D., Pope, F. D., and Rovelli, G.: The viscosity of atmospherically relevant organic particles, https://doi.org/10.1038/s41467-018-03027-z, 2018.

Robinson, A. L., Donahue, N. M., Shrivastava, M. K., Weitkamp, E. A., Sage, A. M., Grieshop, A. P., Lane, T. E., Pierce, J. R.,
740   and Pandis, S. N.: Rethinking Organic Aerosols: Semivolatile Emissions and Photochemical Aging, Science, 315, 1259–1262, https://doi.org/10.1126/SCIENCE.1133061, 2007.

Rush, J. D. and Bielski, B. H.: Pulse radiolytic studies of the reactions of HO2/O2- with Fe(II)/Fe(III) ions. The reactivity of HO2/O2- with ferric ions and its implication on the occurrence of the Haber-Weiss reaction, Journal of Physical Chemistry, 89, 5062–5066, https://doi.org/10.1021/j100269a035, 1985.

745   Schroeder, W. H., Dobson, M., Kane, D. M., and Johnson, N. D.: Toxic Trace Elements Associated With Airborne Pariacnlaie Matter: A Review, https://doi.org/10.1080/08940630.1987.10466321, 1987.

Sedlak, D. L. and Hoigné, J.: The role of copper and oxalate in the redox cycling of iron in atmospheric waters, Atmospheric Environment Part A, General Topics, 27, 2173–2185, https://doi.org/10.1016/0960-1686(93)90047-3, 1993.

Sehested, K., Rasmussen, O. L., and Fricke, H.: Rate constants of OH with HO2, O2-, and H2O2+ from hydrogen peroxide formation in
750   pulse-irradiated oxygenated water, Journal of Physical Chemistry, 72, 626–631, https://doi.org/10.1021/j100848a040, 1968.

Seraghni, N., Belattar, S., Mameri, Y., Debbache, N., and Sehili, T.: Fe(III)-citrate-complex-induced photooxidation of 3-methylphenol in aqueous solution, International Journal of Photoenergy, 2012, https://doi.org/10.1155/2012/630425, 2012.

Shen, J., Griffiths, P. T., Campbell, S. J., Utinger, B., Kalberer, M., and Paulson, S. E.: Ascorbate oxidation by iron, copper and reactive oxygen species: review, model development, and derivation of key rate constants, Scientific Reports 2021 11:1, 11, 1–14, https://doi.org/10.1038/s41598-021-86477-8, 2021.

Shiraiwa, M., Fang, T., Wei, J., Lakey, P. S. J., Hwang, B. C., Edwards, K. C., Kapur, S., Monterrosa Mena, J. E., Huang, Y.-K., Digman, M. A., Weichenthal, S. A., Nizkorodov, S. A., and Kleinman, M. T.: Chemical and Cellular Formation of Reactive Oxygen Species from Secondary Organic Aerosols in Epithelial Lining Fluid, Tech. rep., UCI, 2023.

Silva, A. M., Kong, X., Parkin, M. C., Cammack, R., and Hider, R. C.: Iron(iii) citrate speciation in aqueous solution, Dalton Transactions, pp. 8616–8625, https://doi.org/10.1039/b910970f, 2009.

Steimer, S. S., Berkemeier, T., Gilgen, A., Krieger, U. K., Peter, T., Shiraiwa, M., and Ammann, M.: Shikimic acid ozonolysis kinetics of the transition from liquid aqueous solution to highly viscous glass, Physical Chemistry Chemical Physics, 17, https://doi.org/10.1039/c5cp04544d, 2015.

Tao, Y. and Murphy, J. G.: The Mechanisms Responsible for the Interactions among Oxalate, pH, and Fe Dissolution in PM2.5, ACS Earth and Space Chemistry, 3, 2259–2265, https://doi.org/10.1021/acsearthspacechem.9b00172, 2019.

Tapparo, A., Di Marco, V., Badocco, D., D'Aronco, S., Soldà, L., Pastore, P., Mahon, B. M., Kalberer, M., and Giorio, C.: Formation of metal-organic ligand complexes affects solubility of metals in airborne particles at an urban site in the Po valley, Chemosphere, https://doi.org/10.1016/j.chemosphere.2019.125025, 2020.

Tuet, W. Y., Chen, Y., Fok, S., Gao, D., Weber, R. J., Champion, J. A., and Ng, N. L.: Chemical and cellular oxidant production induced by naphthalene secondary organic aerosol (SOA): effect of redox-active metals and photochemical aging, Scientific Reports 2017 7:1, 7, 1–10, https://doi.org/10.1038/s41598-017-15071-8, 2017.

Virtanen, A., Joutsensaari, J., Koop, T., Kannosto, J., Yli-Pirilä, P., Leskinen, J., Mäkelä, J. M., Holopainen, J. K., Pöschl, U., Kulmala, M., Worsnop, D. R., and Laaksonen, A.: An amorphous solid state of biogenic secondary organic aerosol particles, Nature, 467, 824–827, https://doi.org/10.1038/nature09455, 2010.

von Piechowski, M., Nauser, T., Hoigné, J., and Bühler, R. E.: O2 Decay Catalyzed by Cu2+ and Cu+ Ions in Aqueous Solutions: A Pulse Radiolysis Study for Atmospheric Chemistry, Berichte der Bunsengesellschaft für physikalische Chemie, 97, 762–771, https://doi.org/10.1002/bbpc.19930970604, 1993.

Walling, C.: Fenton's Reagent Revisited, Accounts of Chemical Research, https://doi.org/10.1021/ar50088a003, 1975.

Wang, J., Huang, D., Chen, F., Chen, J., Jiang, H., Zhu, Y., Chen, C., and Zhao, J.: Rapid Redox Cycling of Fe(II)/Fe(III) in Microdroplets during Iron–Citric Acid Photochemistry, Environmental Science & Technology, 57, 4434–4442, https://doi.org/10.1021/acs.est.2c07897, 2023.

Wang, Z., Chen, C., Ma, W., and Zhao, J.: Photochemical coupling of iron redox reactions and transformation of low-molecular-weight organic matter, https://doi.org/10.1021/jz3005333, 2012.

Wei, J., Yu, H., Wang, Y., and Verma, V.: Complexation of Iron and Copper in Ambient Particulate Matter and Its Effect on the Oxidative Potential Measured in a Surrogate Lung Fluid, Environmental Science and Technology, https://doi.org/10.1021/acs.est.8b05731, 2019.

Weichenthal, S., Shekarrizfard, M., Traub, A., Kulka, R., Al-Rijleh, K., Anowar, S., Evans, G., and Hatzopoulou, M.: Within-City Spatial Variations in Multiple Measures of PM2.5 Oxidative Potential in Toronto, Canada, Environmental Science and Technology, 53, 2799–2810, https://doi.org/10.1021/acs.est.8b05543, 2019.

Welch, M. J., Lifton, J. F., and Seck, J. A.: Tracer studies with radioactive Oxygen-15. Exchange between carbon dioxide and water, J. Phys. Chem., 73, 3351–3356, 1969.

Weller, C., Horn, S., and Herrmann, H.: Photolysis of fe(iii) carboxylato complexes: Fe(ii) quantum yields and reaction mechanisms, Journal of Photochemistry and Photobiology A: Chemistry, https://doi.org/10.1016/j.jphotochem.2013.06.022, 2013.

Weller, C., Tilgner, A., Bräuer, P., and Herrmann, H.: Modeling the impact of iron-carboxylate photochemistry on radical budget and carboxylate degradation in cloud droplets and particles, Environmental Science and Technology, https://doi.org/10.1021/es4056643, 2014.

West, C. P., Morales, A. C., Ryan, J., Misovich, M. V., Hettiyadura, A. P., Rivera-Adorno, F., Tomlin, J. M., Darmody, A., Linn, B. N., Lin, P., and Laskin, A.: Molecular investigation of the multi-phase photochemistry of Fe(iii)-citrate in aqueous solution, Environmental Science: Processes and Impacts, https://doi.org/10.1039/d1em00503k, 2023.

Ziajka, J., Beer, F., and Warneck, P.: Iron-catalysed oxidation of bisulphite aqueous solution: Evidence for a free radical chain mechanism, Atmospheric Environment, 28, 2549–2552, https://doi.org/10.1016/1352-2310(94)90405-7, 1994.

795